Partial cavity flows. Part 1. Cavities forming on models without spanwise variation

By K. R. LABERTEAUX AND S. L. CECCIO

Department of Mechanical Engineering and Applied Mechanics, University of Michigan,
Ann Arbor, MI 48109-2121, USA

Partial cavities that formed on the vertices of wedges and on the leading edge of stationary hydrofoils were examined experimentally. The geometry of these test objects did not vary in the spanwise direction (i.e. two-dimensional). Open partial cavities formed on a series of two-dimensional wedges and on a plano-convex hydrofoil. These cavities terminated near the point of maximum cavity thickness, and small vapour-filled vortices were shed in the turbulent cavity wake. The turbulent flow in the wake of the open cavity was similar to the turbulent shear flow downstream of a rearward-facing step. Re-entrant flow was not observed in the cavity closure of open cavities, although recirculating flow associated with a region of flow separation was detected for some cases. Predictions of a two-dimensional free-streamline model of the cavitating wedge flows were compared to the experimentally observed cavities. The model predicted the profile of the open cavity only to the point of maximum cavity thickness. Examination of the flow field near the closure of the open cavities revealed adverse pressure gradients near the cavity closure. The pressure gradients around the open cavities were sufficient to cause large-scale condensation of the cavity. Unsteady re-entrant partial cavities formed on a two-dimensional NACA0009 hydrofoil. The interface of the unsteady closed cavities smoothly curved to form a re-entrant jet at the cavity terminus, and the re-entrant flow was directed upstream. The re-entrant flow impinged on the cavity interface and led to the periodic production of cloud cavitation. These cavities exhibited a laminar flow reattachment. The flow around the closed cavity was largely irrotational, while vorticity was created when the cloud cavitation collapsed downstream of the cavity. Examination of the flow field near closure of these cavities also revealed adverse pressure gradients near the partial cavity closure, but the rise in pressure did not lead to the premature condensation of the cavity.

1. Introduction

Attached or sheet cavitation occurs when a flowing liquid continuously detaches from a solid surface to form a vapour film. A partial cavity closes on the cavitating surface, while a super cavity closes downstream in the wake of the cavitating object. Partial cavitation can be further classified as either *closed* or *open* attached cavitation, depending on the flow in the cavity closure region. A closed partial cavity has a relatively stable cavity length, a clear interface, and a cavity closure that is relatively free of bubbles. An open cavity is typically 'frothy' in appearance, and has a periodically varying length that is associated with the shedding of vapour clouds. The shedding vapour clouds in the closure region of open cavities can range in size from

small vortical structures (i.e. 'streamers', 'horseshoes') to vortices on the scale of the original cavity. When the latter occurs, the open cavity becomes unstable, and large portions of the attached cavity can break off. The large bubbly clouds shed from the cavity are referred to as *cloud cavitation*. Shedding of cloud cavitation is often periodic and can result in large unsteady loads on the cavitating object. Moreover, cloud cavitation can lead to surface erosion and can produce substantial acoustic emissions. Unsteady partial cavitation can result from unsteady flow upstream of the cavitating object. However, cavities that form in steady free-stream conditions can also exhibit significant unsteadiness.

Researchers have shown that a single test object can cavitate with a wide variety of partial cavitation patterns with variation of inlet flow configurations and conditions (see, for example, Franc & Michel 1985). The variety in the reported flows underscores their complexity. Detailed measurements of the cavitating flow field can yield insight into the physical processes underlying the cavitating flow and provide guidance to developers of cavitation models. However, partial cavity flows are often very unsteady, have both liquid and gas phases present, and are characterized by a large range of length and time scales. As a result, measurement of the cavitating flow field is quite challenging. A variety of experimental methods have been used to quantify partial cavity flows. Le, Franc & Michel (1993a,b), Reismann & Brennen (1996), and Larrarte *et al.* (1995) employed mean and dynamic pressure measurements in the vicinity of cavities that formed on two-dimensional hydrofoils, and correlated these measurements to the formation of cloud cavitation. Avellan, Dupont & Ryhming (1988), Kubota *et al.* (1989), and Brewer & Kinnas (1997) employed laser Doppler velocimetry (LDV) to determine the mean and phase-averaged flow field around partial cavities. Maeda, Yamaguchi & Kato (1991) used holography and Pereira (1997) used stereography to examine the cavitating vortical structures that form at the closure of closed cavities on two-dimensional hydrofoils. Kawanami, Kato & Yamaguchi (1998) examined the three-dimensional characteristics of the cavitating vortices that are shed downstream of cavities that formed on two-dimensional hydrofoils, and Laberteaux *et al.* (1998) used high-speed video imaging to examine the collapse of such cavitating vortices. It has been particularly difficult to measure the cavitating flow field. Recently, Zhang, Gopalan & Katz (1998) employed particle imaging velocimetry (PIV) to examine the turbulent flow in the wake of an open partial cavity. Both mean and fluctuating velocity components were measured. Most of these studies examined open cavities that were shedding either small cavitating vortices or large cavitating clouds. Pham, Larrarte & Fruman (1998) and George, Iyer & Ceccio (2000) examined the re-entrant flow within partial cavities using electrical impedance probes.

The formation of cloud cavitation has been the focus of much study with some of the earliest work conducted by Knapp (1955). Knapp used high-speed motion pictures to study the shedding mechanism on axisymmetric bodies. The break-off of the cavity was attributed to a re-entrant jet that formed at the trailing edge of the cavity and moved quickly upstream. When the jet interacted with the cavity interface near the leading edge of the cavity, the cavity separated from the solid surface, and a large vapour cloud was shed and convected downstream. A new cavity then began to grow and the entire process was repeated. Lush & Skipp (1986) also attributed the formation of periodic cloud cavitation to the existence of re-entrant flow. Le *et al.* (1993a) used dye injected near the trailing edge of the cavity to visualize the re-entrant jet convecting upstream to the leading edge of the cavity. They indicate that periodic shedding of clouds requires specific flow conditions (i.e. fluid properties, angle of attack, and pressure conditions). De Lange (1996) used a

transparent two-dimensional hydrofoil to visualize the cavity and also reported that a re-entrant jet is responsible for the cloud generation. Larrarte *et al.* (1995) and Pham *et al.* (1998) also concluded that a re-entrant jet is responsible for the cavity instability they observed. Stutz & Reboud (1997) studied the influence of the internal flow pattern on the unsteady behaviour of cloud cavitation forming at the throat of a converging/diverging nozzle. They use optical probes to detect a reverse flow on the solid surface beneath the attached cavity. Kawanami *et al.* (1997) examined the effect of surface barriers placed on the surface of a two-dimensional cavitating hydrofoil. These barriers were found to substantially modify the re-entrant flow within the cavity.

A variety of definitions have been used in the literature to describe partial cavity types on stationary test objects. We will use the following definitions in subsequent references to partial cavity flows:

Incipient cavity Shear-flow cavitation that forms in a region of pre-existing flow separation. Cavitation occurs in the cores of coherent vortices. The separated region is largely filled with liquid. As the free-stream cavitation number is reduced, a small vapour-filled pocket can occur near the region of flow separation.

Open cavity The cavity near detachment is vapour filled. Downstream of the cavity detachment, the cavity can be filled with a bubbly mixture. The flow closes behind the cavity via a *turbulent* reattachment. *Recirculating* flow may exist in the region of flow separation downstream of the cavity, but *re-entrant* flow is weak and is not spatially coherent along the spanwise extent of the cavity closure. The gaseous cavity contents are shed from the cavity and are entrained into the cores of the vortices in the turbulent shear flow downstream of the cavity. The length scale of the cavitating vortices is on the order of the length scale of the largest coherent vortices in the turbulent wake.

Unsteady re-entrant cavity The cavity is largely vapour filled, the cavity interface closes back at the cavity terminus to form a thin re-entrant flow. The flow closes behind the cavity via a laminar reattachment. The re-entrant flow locally impinges on the cavity interface causing periodic break-off and roll-up of a portion of the cavity. If the re-entrant jet moves far upstream to cause a large portion of the cavity to break off, the process creates *large-scale cloud cavitation*. If the re-entrant flow moves a small distance upstream before impingement on the cavity surface, then the process creates *small-scale cloud cavitation*.

In the present study, we examined partial cavity flows over stationary test objects with geometries that do not vary in the spanwise direction (i.e. two-dimensional test objects). Three types of two-dimensional test objects were examined: wedges, a plano-convex hydrofoil, and a NACA0009 series hydrofoil. Incipient cavities were examined on all of the test objects under certain conditions. As partial cavities developed on the wedges and on the plano-convex hydrofoil, open cavities were observed. In contrast, only unsteady re-entrant cavities developed on the NACA0009 hydrofoil. The flows near the closure region of these cavities were examined in order to reveal the origin of these different developed cavities. In addition, results from a two-dimensional analytical model of the partial cavities on the wedge were compared with the observed open cavities.

2. Experimental methods

The experiments described here were conducted in the Cavitation and Multiphase Flow Laboratory at the University of Michigan, Department of Mechanical Engi-

neering and Applied Mechanics. Several techniques were employed for qualitative and quantitative flow analysis, including flash photography, particle streak photography (PSP), single-frame particle image velocimetry (PIV), and cinemagraphic PIV. These techniques, along with the experimental apparatus and test models, are described below. Detailed descriptions of the experimental setup and methods are found in Laberteaux (1998).

2.1. *Blow-down water tunnel*

Controlled cavitation experiments were conducted in the blow-down water tunnel (BDWT), and a description of this facility is provided in Tassin *et al.* (1995). The BDWT consists of two $1.5\,\text{m}^3$ tanks that are connected through a square contraction (area ratio $4.4:1$), a test section, and a diffuser. The test section has a $76.2\,\text{mm}$ square cross-section and a length of $260\,\text{mm}$. Four removable windows are constructed of either polycarbonate to allow optical access or aluminium to mount the test objects.

The free and dissolved air content of the BDWT can be qualitatively controlled through de-aeration, and by allowing free gas bubbles to reach the free surfaces in the two tanks. The quantity and characteristics of free-stream nuclei relate directly to the cavitation susceptibility of the fluid, and affect both the inception and development of cavitation. However, the development of partial cavitation is less sensitive to the free-stream nuclei content (see, for example, Gindroz & Billet 1994). In the present study, both the free and dissolved gas contents were qualitatively controlled. The dissolved gas content was controlled through de-aeration of the water in the BDWT. Prior to testing, a de-aeration loop was initiated, where the free surfaces of the tanks were exposed to vacuum pressure. The dissolved gases were absorbed when the water was sprayed into the top portion of the lower tank, creating more interfacial area exposed to vacuum. The de-aeration system was capable of reducing the oxygen content of fresh water (approximately 80% saturation) to 30% saturation. The water in the BDWT was allowed to settle between tests as it rested in the upper tank prior to blow-down. This allowed free gas bubbles to rise to an evacuated free surface, and holographic examination of the flow indicates that this procedure eliminated free gas bubbles with diameter greater than $5\,\mu\text{m}$ (Yu & Ceccio 1997).

During an experiment, water was drawn into the upper tank and then forced through the test section and into the lower tank. Controlled application of pressure and vacuum to the two tanks was employed to produce the desired flow in the test section. The initial starting pressure of a test was set independently of the velocity of the fluid, allowing the study of both cavitating and non-cavitating flows at the same speed. Absolute and differential pressure transducers were used to measure the test-section static pressure and velocity, respectively. Calibration of the tunnel velocity was performed with an independent laser Doppler velocimeter measurement.

2.2. *Test models*

Wedges and hydrofoils without spanwise variation were used in this study. Three different two-dimensional wedges with vertex angles β of $26.5°$, $20.5°$, and $14°$ were employed, all with a step height of $19\,\text{mm}$. The wedges were mounted directly onto a custom-made test-section window, and no effort was made to control the wall-bounded flow that formed upstream of the wedge. A plano-convex hydrofoil was constructed with a flat suction side and a curved pressure side. The radius of the pressure side was $184\,\text{mm}$, the maximum thickness of $12.7\,\text{mm}$ was at 50% chord, and the leading-edge radius was $1.6\,\text{mm}$. This geometry was chosen to achieve separation near the leading edge of the foil. The cavity patterns that can form on this hydrofoil geometry are

described by Le *et al.* (1993*a*, *b*). A two-dimensional NACA0009 hydrofoil was also examined. The chord length of the hydrofoil was 127 mm and the width was 78 mm. The maximum thickness was 11.4 mm, and was located at 30% of the chord from the leading edge. The NACA0009 was selected for its non-separating fully wetted flow, and this section has been examined by Kawanami *et al.* (1998). All of the wedges and hydrofoils spanned the width of the test section to minimize gap flows. The hydrofoils were mounted on an arbour that allowed the hydrofoils to be placed at an attack angle. All test objects were made of brass and were highly polished.

Rearward-facing steps with step heights of 0.16 cm, 0.32 cm, and 0.64 cm were constructed and tested in the BDWT to determine reattachment lengths behind the steps for comparison with the partial cavities that formed on the two-dimensional wedges. A 26.5° wedge was used upstream of the step to provide a streamlined inflow.

2.3. *Flash photography and particle streak photography* (*PSP*)

A 35 mm Nikon camera and a Strobolume strobe-scope system were employed to study the detailed structure and evolution of attached cavitation formed on the different test models. The camera, using Kodak professional 400-speed colour film or Kodak TMAX 400 black-and-white film, was used to capture the front view of the partial cavities. Particle streak photography (PSP) was used to visualize the streamlines in the non-cavitating and cavitating flows. The flow was seeded with fluorescent latex particles with an average diameter of 30 μm. An Nd–YAG laser (~ 6 W maximum power at 532 nm) was used to create a continuous light sheet. The camera was equipped with a filter to block the scattered laser light ($\lambda = 532$ nm) while recording the fluorescent return of the particles.

2.4. *Single-frame, double-pulsed particle imaging velocimetry* (*PIV*)

Single-frame, double-pulsed particle imaging velocimetry (PIV) was used to investigate the non-cavitating and the cavitating flow filed. PIV can be used to non-intrusively visualize large regions of a flow field with substantial spatial and temporal resolution. Application of PIV to multiphase flows has been discussed by Adrian (1991), Liu & Adrian (1993), and Sridhar & Katz (1994).

The flow was seeded with fluorescent latex particles with an average diameter of 30 μm. Seeding the flow with particles did not result in the addition of active cavitation nuclei. By employing fluorescent particles, it was possible to distinguish Lagrangian flow tracers from the small bubbles present downstream of the cavity closure. The output of two frequency-doubled Quanta Ray Nd–Yag GCR130 lasers was directed through an optical assembly to create a sheet of light with thickness ~ 1 mm. The lasers have a design repetition rate of 30 Hz with a maximum energy of 100 mJ in a 7 ns pulse. Double-pulsed images were captured with a 35 mm Nikon camera equipped with a filter to block the scattered laser light ($\lambda = 532$ nm), while recording the fluorescent return of the particles ($\lambda = 580$ nm). An oscillating mirror system (General Scanning Inc.) was used to impose an image shift in the direction of the free stream, eliminating directional ambiguity inherent in single-frame, double-pulsed images.

The double-pulsed images recorded on the photographs were digitized (at 2700 d.p.i. using a Nikon LS-1000 35 mm film scanner) and processed to determine the spacing between the particle pairs. The thickness of the light sheet was sufficient to prevent tracer particles from leaving the sheet between the two pulses of the laser. The vector fields were reconstructed from the filtered images using the software packages VISIFLOW (AEA Technology, PLC) and INSIGHT (TSI Inc.). Autocorrelation
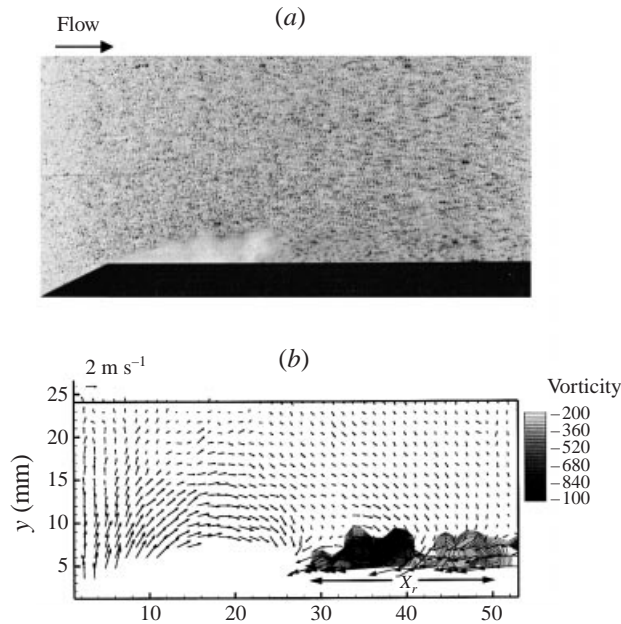
Flow →   (*a*)

(*b*)

FIGURE 1. (*a*) Double pulsed PIV image, and (*b*) resulting plot of vorticity. $U_\infty = 8.5\,\mathrm{m\,s^{-1}}$ and $\sigma = 2.2$. x_r is the region of high vorticity behind the cavity.

was employed to analyse the PIV images (see Dong, Chu & Katz 1992 for a detailed description). The autocorrelation routine in both software packages attained sub-pixel accuracy on the location of the correlation peak by using a Gaussian optimization routine to find the correlation peak. Velocity vectors were determined close to the solid surfaces and the gas/liquid interfaces of the bubbles. The size of the interrogation window was 128×128 pixels, resulting in an analysis resolution of approximately 1.5 mm based on the magnification of the image. The interrogation window was overlapped 50% to obtain a distance of approximately 0.75 mm between vectors. The image shift for the single-frame images was introduced during post-processing of the images. In addition, the validity of the vectors could be checked manually or automatically within the PIV software packages. Approximately 5% of the original velocity vectors were eliminated during vector field validation. The out-of-plane component of vorticity and the instantaneous in-plane streamlines were computed from the two-dimensional velocity data. Figure 1(*a*) presents a single, unprocessed PIV image of a cavity near the wedge, and figure 1(*b*) shows the velocity vectors with the mean velocity subtracted, along with vorticity contours.

2.5. *Cinemagraphic PIV*

A double-pulsed, multiple-frame PIV system was developed that has the capability of capturing a series of consecutive images at a high repetition rate (10 000 frames per second). Double-pulsed images were preferred to frame-to-frame images to eliminate errors in the velocity measurement that can result from frame-to-frame registration errors. Two Clark MXR ORC-1000 fast-flashing Nd–YAG lasers (30 kHz maximum repetition rate), and a Photec 16 mm high-speed rotating prism camera (10 kHz maximum framing rate) were used. 100 ft rolls of KODAK 7222 black-and-white reversible negative film were used to record the images. A framing rate of 2000 frames $\mathrm{s^{-1}}$ was used to capture the evolution of the shedding cavitation. At this

framing rate, the film velocity was $50\,\text{ft}\,\text{s}^{-1}$, and the test time for exposing an entire roll of film was approximately $2\,\text{s}$. No image shift was employed during the acquisition of the double-pulsed images. Thus, directional ambiguity was not resolved in the streamwise direction. Before acquiring data with the cinemagraphic PIV system, image-shifted single-shot PIV images were acquired and analysed to identify regions of strong reverse flow. Cinemagraphic data were only collected for flows that did not exhibit flow reversal.

The photographic images were digitized at 2700 d.p.i. using a Nikon LS-1000 $35\,\text{mm}$ film scanner with a film mask so that the $16\,\text{mm}$ film lay flat in the film holder, the sprocket holes on the film were used for registration from image to image, and the size of each image was carefully measured. The vector fields reconstructed from the filtered images were obtained using the software package INSIGHT (TSI Inc.). To analyse the PIV images, autocorrelation was employed, which attained sub-pixel accuracy on the location of the correlation peak by using a Gaussian optimization routine to find the correlation peak. Velocity vectors were determined close to the solid surfaces and the gas/liquid interfaces of the bubbles. The size of the interrogation window was 64×64 pixels, resulting in an analysis resolution of approximately $2.5\,\text{mm}$ based on the magnification of the image. The interrogation window was overlapped 50% to obtain a distance of approximately $1.5\,\text{mm}$ between vectors.

2.6. *Experimental uncertainty*

The uncertainty in the experimentally determined parameters has been estimated. The free-stream velocity and pressure were known to within $\pm2\%$ and $\pm1\%$, respectively. This produces an error in the free-stream cavitation number of $\pm6\%$ over the range of free-stream conditions tested.

The measurement uncertainty in the photographic image magnification was $\pm2\%$. Measurement precision of dimensions on the digitized photographs was limited by the digitizing resolution of the scanned image. PSP images were scanned with a resolution of 600 d.p.i. and 2700 d.p.i., whereas PIV images were scanned with a resolution of 2700 d.p.i. Spatial dimensions measured from the streak images have an uncertainty of $\pm5\%$, excluding the measurement of the turbulent reattachment length, which has an uncertainty of $\pm10\%$.

The uncertainty in the final correlated velocity was related to uncertainty in the spatial and temporal measurements of the system. The time interval between successive laser light pulses was very precisely controlled, and known within $50\,\text{ns}$. The uncertainty in the measured time interval was less than $\pm0.1\%$. The uncertainty in the spatial data was largely related to the magnification of the image and the size of the PIV autocorrelation interrogation window. The uncertainty in the velocity vector that was determined through autocorrelation can be assessed through evaluation of the signal-to-noise ratio between the largest correlated peak and the other peaks found. A variety of criteria were used to validate the individual vectors. The vector field was post-processed to eliminate spurious vectors through a comparison with the surrounding (or field-averaged) vectors. In addition, a manual process was used to compare the computed vectors with the underlying particle-pair image. Approximately 5% of the original velocity vectors were eliminated during the vector field validation. For single-frame PIV, the uncertainty in the image shift velocity must be included. For cinemagraphic PIV, uncertainty in the registration of the image must be considered. An estimate can be made of the overall uncertainty for the PIV-derived velocity data. For single-shot PIV, it was estimated that the average uncertainty of the velocity was $\pm2\%$; and for the cinemagraphic PIV, the average uncertainty of the

velocity was $\pm 5\%$. Note that the uncertainty in the cross-stream component of the velocity vector will be a higher percentage of the cross-stream velocity value.

3. Results: partial cavities forming of the wedges and the plano-convex hydrofoil

Partial cavities formed at the vertex of each of the three wedges and the leading edge of the plano-convex hydrofoil. The nominal free-stream velocity for the wedge experiments was $9.0 \pm 0.3\,\mathrm{m\,s^{-1}}$, the average free-stream Reynolds number based on cavity length, Re_c, was equal to $(6.6\pm2.3)\times10^4$, and the free-stream cavitation number, σ, varied between 2.2 and 1.6. The nominal free-stream velocity for the plano-convex hydrofoil experiments was $9.5 \pm 1.0\,\mathrm{m\,s^{-1}}$, making the free-stream Reynolds number based on the hydrofoil chord length, $Re_L = U_\infty L/v$, equal to $(1.1\pm0.1)\times10^6$. The angle of incidence, α, varied from $1°$ to $5°$. PSP was used to visualize the flow field around the cavity and to measure the cavity geometry. Single-shot PIV was used to determine the flow field around and behind the partial cavity. The region of high vorticity downstream of the two-dimensional cavity was compared to the reattachment zone behind a rearward-facing step.

3.1. Non-cavitating flow

The non-cavitating flow near the vertex of the two-dimensional wedge was examined with PSP, and a typical PSP image is shown in figure 2(a), revealing flow separation at the vertex of the wedge. This separation bubble was examined for the three wedges, and the ratio of bubble thickness to length was approximately $h_S/L_S = 0.15 \pm 0.03$.

The non-cavitating flow near the leading edge of the two-dimensional plano-convex hydrofoil was also examined using PSP. Figures 3(a) and 4(a) show images of the flow for $\alpha = 2°$ and $5°$, respectively. Flow separation was detected near the hydrofoil leading edge. As the attack angle was increased, the length and thickness of the separation bubble increased. Figure 5 presents a plot of the separation bubble thickness, h_S, versus the bubble length, L_S, for a range of hydrofoil attack angles. The ratio of the separation bubble thickness to bubble length was approximately constant with $h_S/L_S = 0.13 \pm 0.03$.

3.2. Cavity inception and appearance

As the free-stream pressure was lowered, incipient cavities formed near the vertex of the wedge in the region of non-cavitating flow separation. Figure 6(a) illustrates a typical incipient cavity on the $20.5°$ wedge. Continued lowering of the pressure results in an open partial cavity that is a frothy mixture as shown in figures 6(b) and 6(c). Bubbles and vortical structures were shed downstream of the cavity and subsequently collapsed. Figures 2(b) and 2(c) show streak photography images of the cavity as it formed on the $20.5°$ wedge. The cavity first appeared when vapour filled the small region of flow separation. The original region of flow separation became completely filled with vapour with decreasing static pressure (cavitation number), and the cavity grew beyond the extent of the original separated region. These developed cavities were filled with a liquid/vapour mixture for most of the cavity length. The flow in the cavity closure region was turbulent, even for partial cavities of nominally constant length. The unsteadiness of the streamline reattachment region can be visualized in the PSP images. Vapour from the cavity was rolled up into vortical flow structures that were convected downstream (Laberteaux et al. 1998).

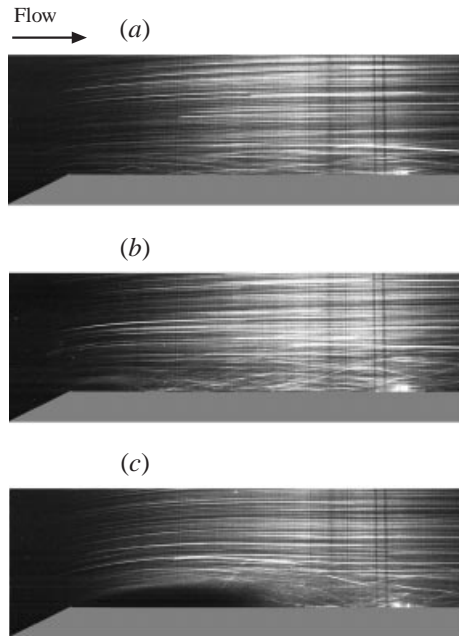Similar cavities were observed at the leading edge of the plano-convex hydrofoil.

Flow → (*a*)

(*b*)

(*c*)

FIGURE 2. Streak photography images of cavitation forming at the vertex of the two-dimensional wedge. (*a*) $U = 8.6 \, \mathrm{m \, s^{-1}}$, $\sigma = 3.1$ (non-cavitating); (*b*) $U = 9.1 \, \mathrm{m \, s^{-1}}$, $\sigma = 2.4$; (*c*) $U = 9.6 \, \mathrm{m \, s^{-1}}$, $\sigma = 1.8$. The streamwise extent of the image is approximately 5 cm.

Attached cavitation formed on the suction side of the hydrofoil near the leading edge as the static pressure was lowered. The process of cavity inception differed for cases of low and high attack angles. For low attack angles ($\alpha \leqslant 3°$), the cavity first appeared when vapour filled the small region of flow separation. With decreasing static pressure (cavitation number), the original region of flow separation became completely filled with vapour, and the cavity began to grow beyond the extent of the original separated region. These developed cavities were vapour-filled near the point of cavity detachment, but were filled with a liquid/vapour mixture for most of the cavity length. Vapour-filled vortices were shed downstream of the cavity, and therefore, the cavities were open. Figure 7 shows three images of cavities forming on the hydrofoil for $\alpha = 2°$. For higher attack angles ($\alpha > 3°$), inception of cavitation occurred within the vortices of the shear layer that existed at the boundary of the separation bubble. Both spanwise and streamwise vortices were visualized as vapour filled their cores. As the pressure was decreased, the separation bubble filled with a liquid/vapour mixture. Near the point of cavity detachment, the cavity was vapour-filled. Figure 8 shows three images of cavities forming on the hydrofoil for $\alpha = 5°$. The cavitating shear layer is easily seen in figure 8(*a*).

Figures 3 and 4 show streak photography images of the cavitation as it formed on the two-dimensional plano-convex hydrofoils for attack angles of 2° and 5°, respectively. The cavity first appeared when vapour filled the small region of flow separation. For low attack angles, the cavity filled the separation bubble and grew beyond the separated region. At higher angles of attack, the cavities did not grow beyond the separated region of the fully wetted flow. In both cases, the developed cavities were filled with a liquid/vapour mixture for most of the cavity length. The flow in the cavity closure region was very unsteady, even for partial cavities of
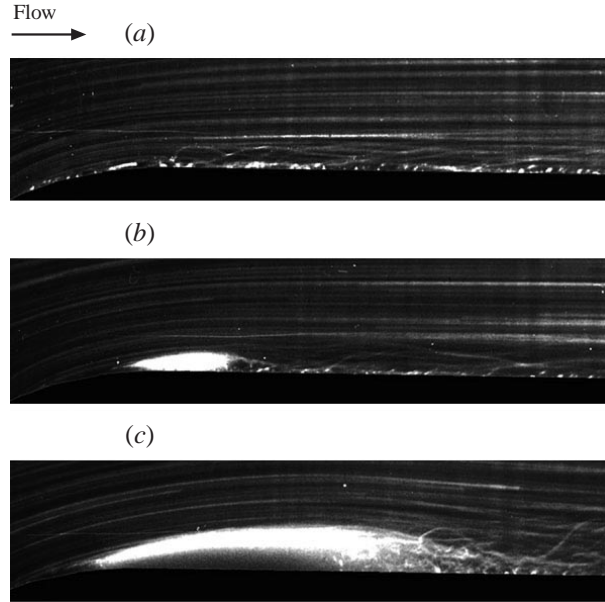
Flow

(a)

(b)

(c)

FIGURE 3. Streak photography images of cavitation forming at the leading edge of the two-dimensional, plano-convex hydrofoil at $\alpha = 2°$. (a) $U = 9.2\,\mathrm{m\,s^{-1}}$, $\sigma = 1.4$ (non-cavitating); (b) $U = 9.5\,\mathrm{m\,s^{-1}}$, $\sigma = 1.2$; (c) $U = 9.5\,\mathrm{m\,s^{-1}}$, $\sigma = 1.0$. The streamwise extent of the image is approximately 1 cm.

nominally constant length. The unsteadiness in the closure of the two-dimensional cavities was a product of the unsteadiness in the turbulent separated flow downstream of the cavity.

3.3. *Cavity geometry*

The length and thickness of the cavities forming at the vertex of the wedge increased with decreasing cavitation number. Figure 9(a) shows the cavity length as a function of the cavitation number, and figure 9(b) shows the cavity length as a function of cavity thickness. The curves also presented will be described below. Similarly, figure 10 presents the cavity thickness versus length for cavities at the leading edge of the plano-convex hydrofoil. The solid lines represent the data for the non-cavitating separation bubble, $h_S/L_S = 0.13 \pm 0.03$. Cavities forming at higher attack angles were shorter than the length of the original separation bubble. Also plotted on the figure is the sum of the cavity length and the length of the flow reattachment downstream of the cavity for $\alpha = 5°$. The reattachment length is the length of the high-vorticity region downstream of the cavity as measured from the PSP images. These data show that the dimensions of the cavitating separated bubble were qualitatively similar to those of the non-cavitating separated flow.

3.4. *Flow near the cavity and in the closure region*

A series of cinemagraphic PIV images of the partial cavity flow were acquired, and individual images were selected in order to phase-average the velocity data. The double-pulsed images were chosen such that the length and geometry of the partial cavity was similar for all the images. Figure 11(a) presents the averaged velocity field for a series of 50 images of cavities on the two-dimensional 26.5° angle wedge. The cavity geometry was selected such that the closure of the cavity was
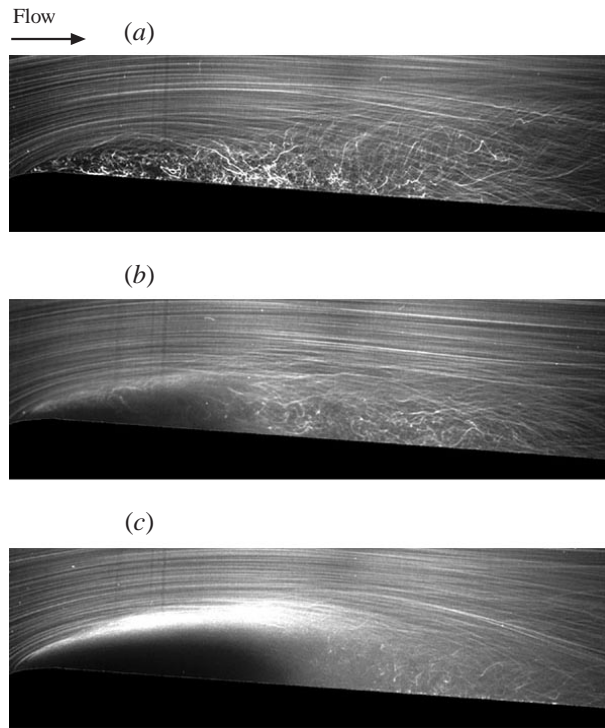
Flow →

(a)

(b)

(c)

FIGURE 4. Streak visualization images of cavitation forming at the leading edge of the two-dimensional plano-convex hydrofoil at $\alpha = 5°$. (a) $U = 8.6\,\mathrm{m\,s^{-1}}$, $\sigma = 3.5$ (non-cavitating); (b) $U = 9.5\,\mathrm{m\,s^{-1}}$, $\sigma = 2.3$; (c) $U = 9.6\,\mathrm{m\,s^{-1}}$, $\sigma = 1.9$. The streamwise extent of the image is approximately 5 cm.
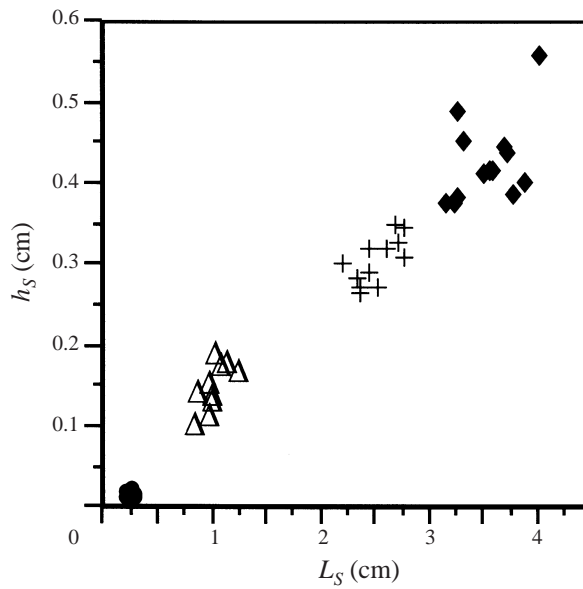
FIGURE 5. Plot of the separation bubble thickness, h_S, versus separation bubble length, L_S, for varying attack angles on the plano-convex hydrofoil ●, $\alpha = 2°$; △, $\alpha = 3°$ +, $\alpha = 4°$; ◆, $\alpha = 5°$.

(*a*)

(*b*)

(*c*)
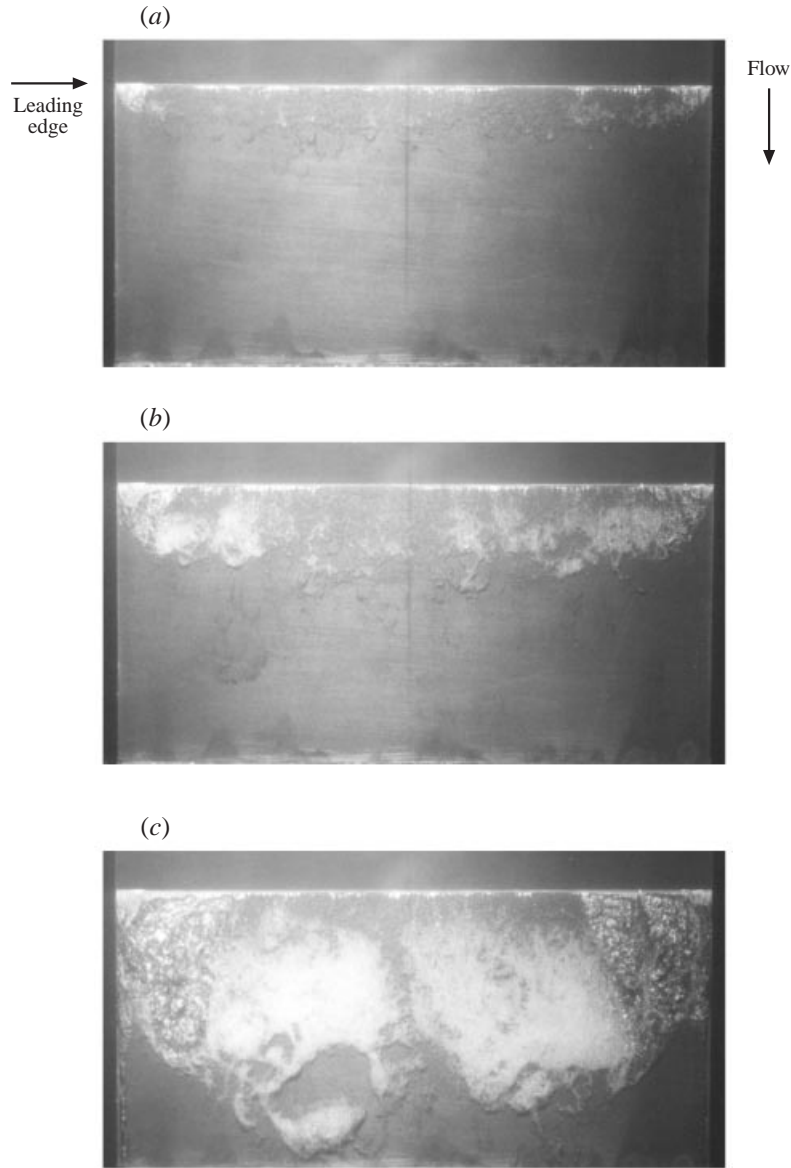
FIGURE 6. Cavitation on the two-dimensional, 20.5° wedge. (*a*) $U = 9.2\,\mathrm{m\,s}^{-1}$, $\sigma = 1.8$; (*b*) $U = 9.5\,\mathrm{m\,s}^{-1}$, $\sigma = 1.6$; (*c*) $U = 9.5\,\mathrm{m\,s}^{-1}$, $\sigma = 1.4$. The span of the wedge is 7.62 cm.

temporarily free of large bubble clouds. The cavity boundary was conservatively defined to eliminate the portions of the image containing vapour and/or distorted particle images. Recirculating flow was not observed in the cavity wake. Figure 11(*b*) shows the velocity field with the average velocity subtracted, and figure 11(*c*) presents the corresponding averaged vorticity plot. The flow remained largely irrotational upstream of the cavity closure, whereas a vortical wake was visualized downstream of the cavity. Distinct regions of concentrated negative vorticity appeared in the wake of the cavity, even after averaging. This suggests that the collapse of the vortical structures downstream of the cavity produced a local region of highly vortical flow.
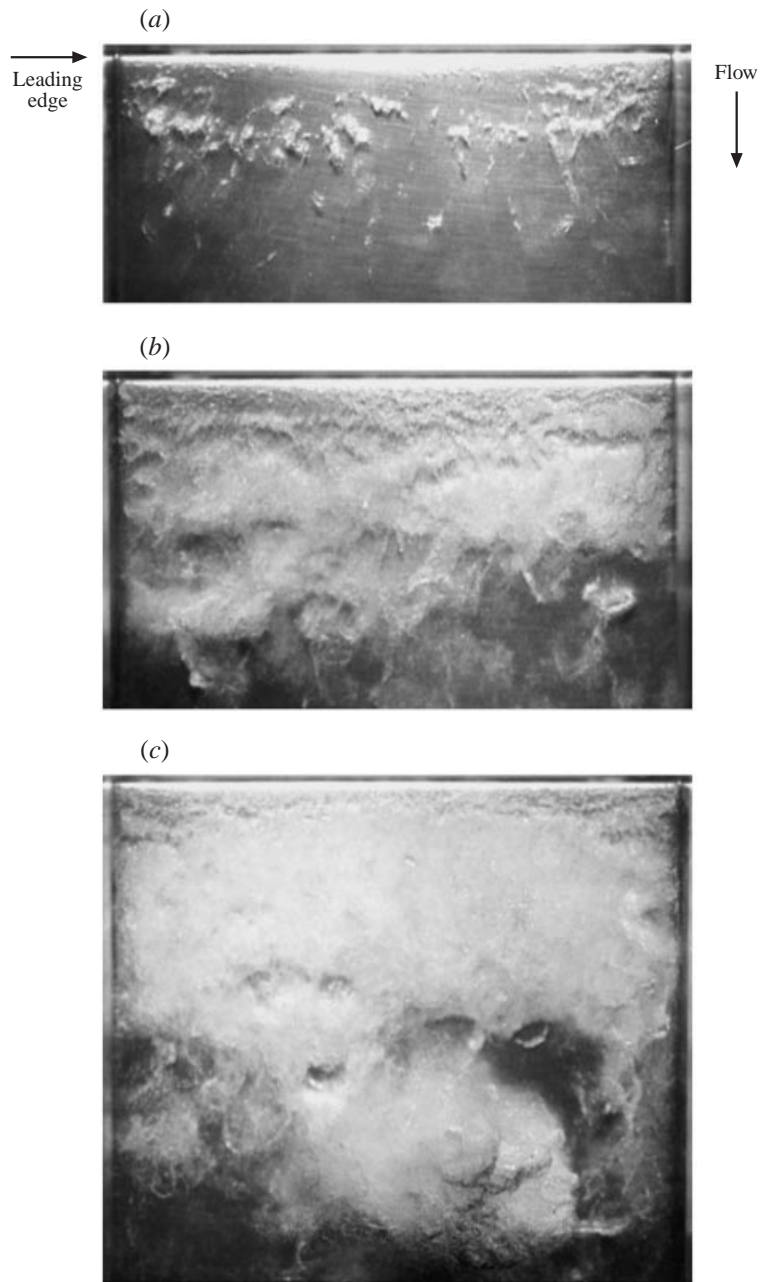
(*a*)

Leading
edge

Flow

(*b*)

(*c*)
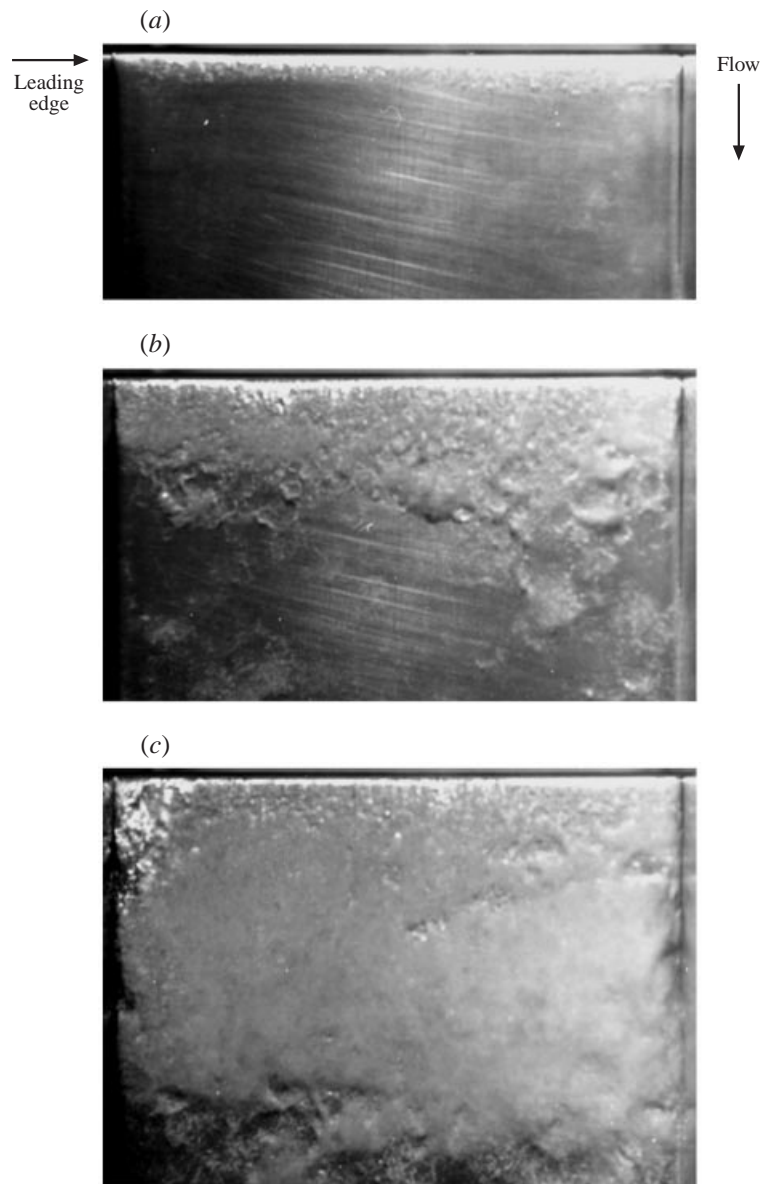
FIGURE 7. Cavitation on the two-dimensional, plano-convex hydrofoil at $\alpha = 2°$. (*a*) $U = 9.2\,\mathrm{m\,s^{-1}}$, $\sigma = 0.8$; (*b*) $U = 9.5\,\mathrm{m\,s^{-1}}$, $\sigma = 0.63$; (*c*) $U = 9.4\,\mathrm{m\,s^{-1}}$, $\sigma = 0.6$. Plan view.

The vortices collapsed at approximately the same downstream location, and this region of highly vortical fluid convected downstream. Thus, the phase-averaged image showed a series of high-vorticity regions since the shedding process was quasi-periodic. The turbulent wake behind the cavity had a thickness on the order of the maximum cavity thickness.

Figure 11(*d*) shows a contour plot of the square of the local average flow speed, $|\boldsymbol{u}|^2 = u^2 + v^2$. Because the flow was largely irrotational near the cavity interface, the local pressure was found from the local speed through application of the Bernoulli equation. It was assumed that the steady Bernoulli equation can be employed in this

(*a*)

(*b*)

(*c*)

FIGURE 8. Cavitation on the two-dimensional, plano-convex hydrofoil at $\alpha = 5°$. (*a*) $U = 9.1\,\mathrm{m\,s^{-1}}$, $\sigma = 2.2$; (*b*) $U = 9.6\,\mathrm{m\,s^{-1}}$, $\sigma = 1.7$; (*c*) $U = 9.6\,\mathrm{m\,s^{-1}}$, $\sigma = 1.5$. Plan view.

steady region of the flow. Consequently, the square of the local speed was related to the local pressure by $(1 - C_P) \approx |\boldsymbol{u}|^2 / U_\infty^2$, where $C_P = P - P_\infty / \frac{1}{2}\rho U_\infty^2$ was the local pressure coefficient. The pressure near the cavity surface reached a minimum near the middle of the cavity, where an adverse pressure gradient was observed. The pressure rose as the cavity terminus was reached.

Fluctuating components of the flow field were also determined for the series of 50
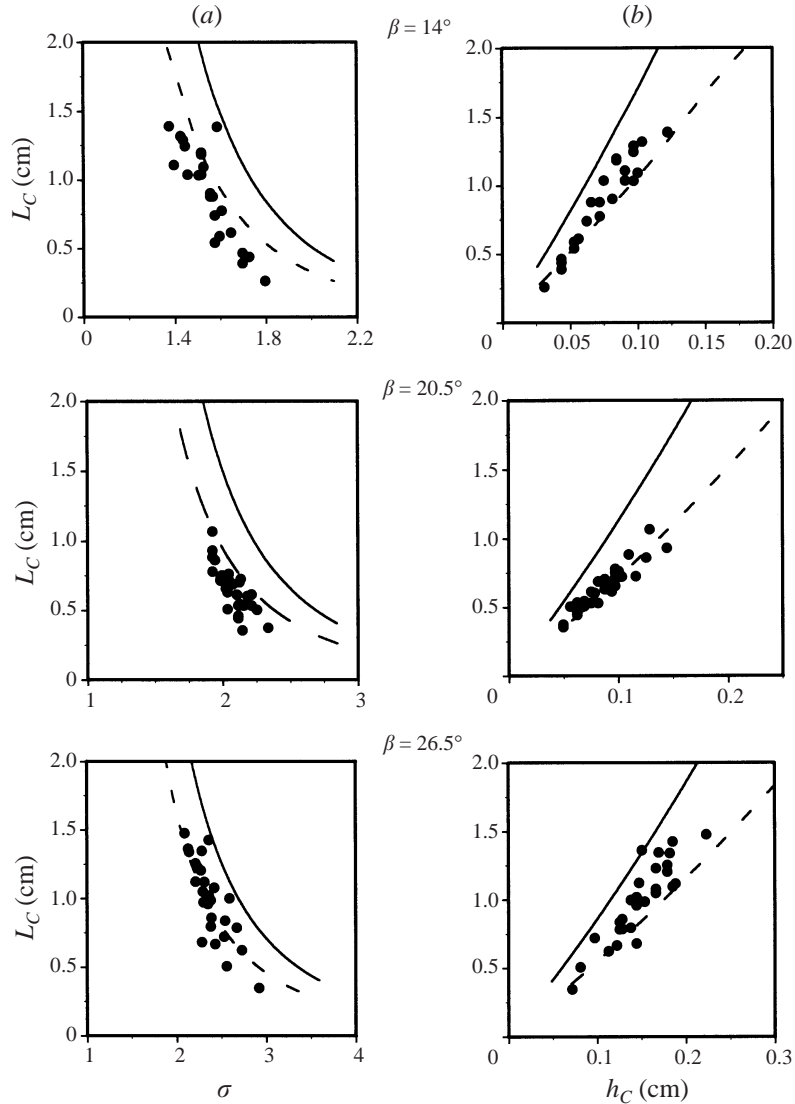
FIGURE 9. (*a*) Cavity length, L_C, as a function of the cavitation number, σ, and (*b*) as a function of cavity thickness, h_C. Also plotted are the analytical solution for the cavity thickness, the maximum cavity length (solid line) and the length at the point of maximum thickness (dashed line). Data are shown for the 14°, 20.5°, and 26.5° wedges. Uncertainties: $\sigma \pm 6\%$, $L_C \pm 5\%$.

images. Figure 12(*c*) details a square region of the PIV image where the average *u* velocity component was measured, and the flow field in each image was normalized with this 'outer flow' velocity, u_o. This was done to minimize the effect of free-stream velocity fluctuations on the determination of the unsteady data. The average velocity at each vector location was determined, and this local average was subtracted from each vector to determine the fluctuating velocity components, $(u/u_o)'$ and $(v/u_o)'$. These data were then used to determine the average Reynolds stresses, $\overline{(u/u_o)'(u/u_o)'}$, $\overline{(v/u_o)'(v/u_o)'}$, and $\overline{(u/u_o)'(v/u_o)'}$. The unsteadiness due to turbulence in the free-stream was small, but the average free-stream velocity decreased by 2% during the data
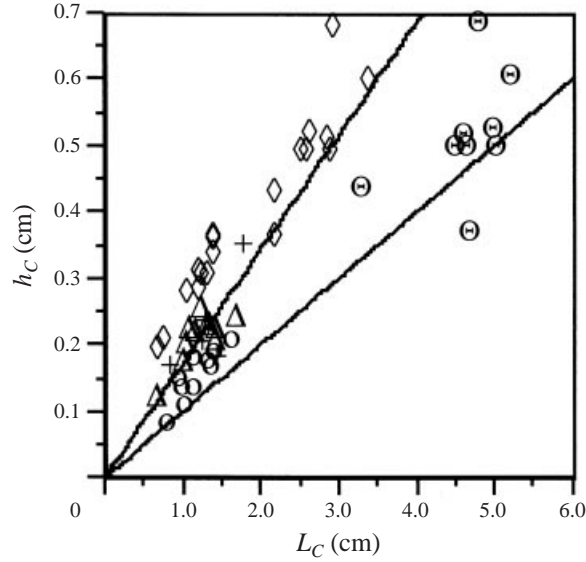
FIGURE 10. Plot of the cavity thickness, h_C, versus cavity length, L_C, for varying attack angles on the plano-convex hydrofoil. O, $\alpha = 2°$; Δ, $\alpha = 3°$; +, $\alpha = 4°$; $\diamond$, $\alpha = 5°$. Also plotted is the cavity thickness versus the sum of the cavity length and reattachment length at $\alpha = 5°$ (Θ). The solid lines represent the data for the non-cavitating separation bubble, $h_S/L_S = 0.13 \pm 0.03$.

acquisition process. By scaling the vector field with an outer flow velocity determined within the vector field, this global unsteadiness in the free stream can be minimized. Figures 12(a), 12(b), and 12(c) present plots of the average Reynolds stresses. Again, the turbulent fluctuations were the largest in the wake of the cavity.

Fifty images were used to determine the fluctuating quantities, which is small compared to the number of samples required to obtain a stationary mean. Figure 13 demonstrates the convergence of the Reynolds stresses at an arbitrary point located within the turbulent flow downstream of the cavity. These data suggested that the average flow quantities continued to change with the averaging of only 50 data sets, which agreed with Zhang et al. (1998). However, the variations in the turbulence parameters became less significant with a sampling of 50 images, and qualitative flow features can be determined from the present data.

The flow around the partial cavities that occurred at the leading edge of the plano-convex hydrofoil were also examined with single-shot and cinemagraphic PIV. For the low attack angle condition, the cavities were thin and the flow in the closure did not recirculate. Analysis of many instantaneous images did not reveal flow in the upstream direction. However, recirculation was seen within the closure region flow for the high attack angle cases. In cases where recirculation was observed, the cavity did not fill the original non-cavitating separation bubble, and therefore, the reverse flow that was observed was due to recirculation in the separation bubble. A turbulent shear flow was observed in the wake of both cavities. The magnitude of the vorticity in the wake of the thicker cavity was similar to that of the non-cavitating separated flow.

The flow in the cavity closure was very unsteady and three-dimensional, even for a cavity of nominally constant length. The shedding of the small cavitating vortices was quasi-periodic, with a shedding frequency, f_S, of approximately 300 to 400 Hz. The Strouhal number of cavity shedding was then $St = f_S L_C / U_\infty \sqrt{1 + \sigma} \approx 0.3\text{--}0.4$.
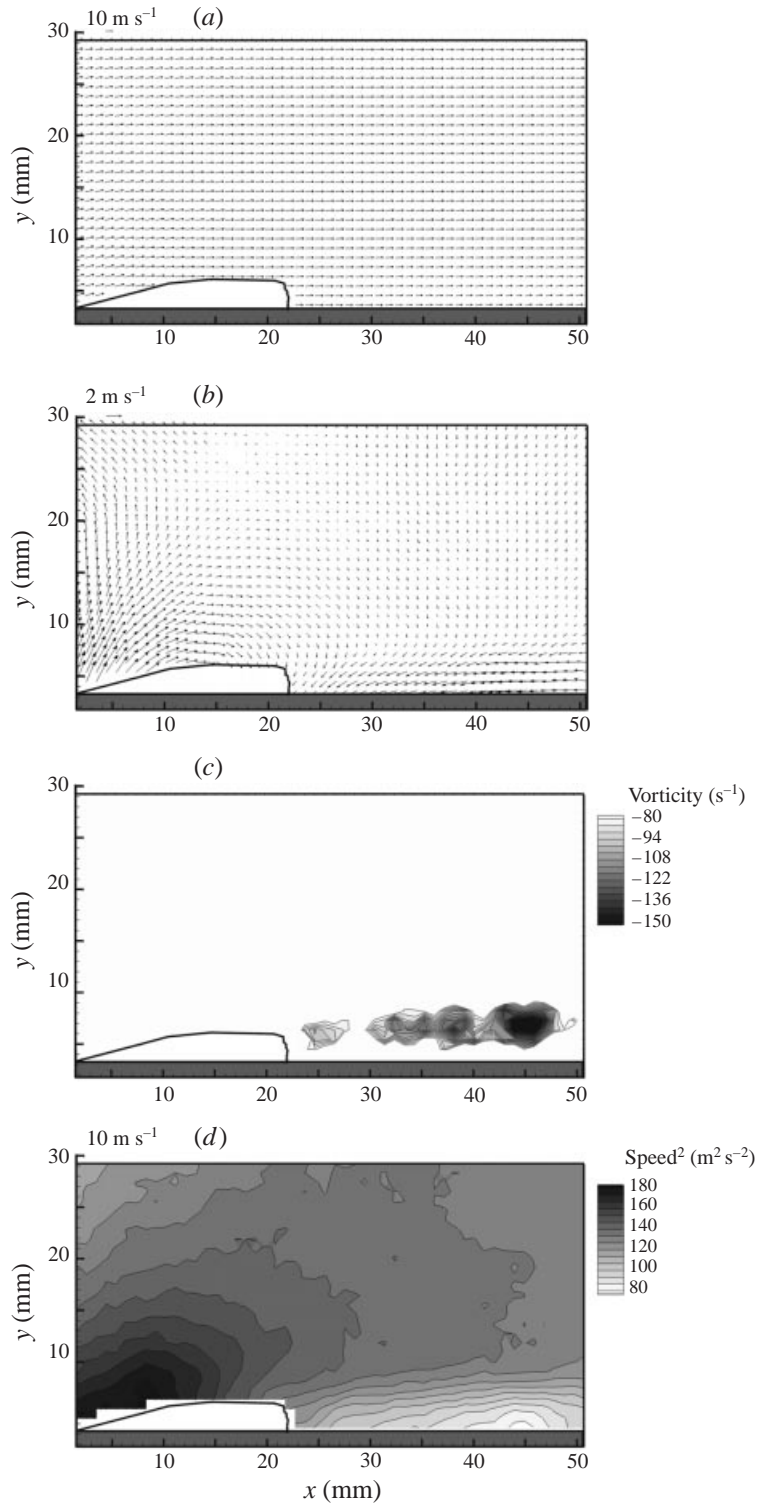
FIGURE 11. Phased average of 50 PIV velocity vector fields on the two-dimensional wedge. $\beta = 26.5°$, $U = 8.4\,\mathrm{m\,s^{-1}}$, $\sigma = 1.9$. (*a*) Velocity field and (*b*) velocity field with the global mean subtracted, $U_{gm} = 11.6\,\mathrm{m\,s^{-1}}$, $V_{gm} = 1.1\,\mathrm{m\,s^{-1}}$; (*c*) vorticity field, and (*d*) flow speed $|\boldsymbol{u}|^2 = u^2 + v^2$.
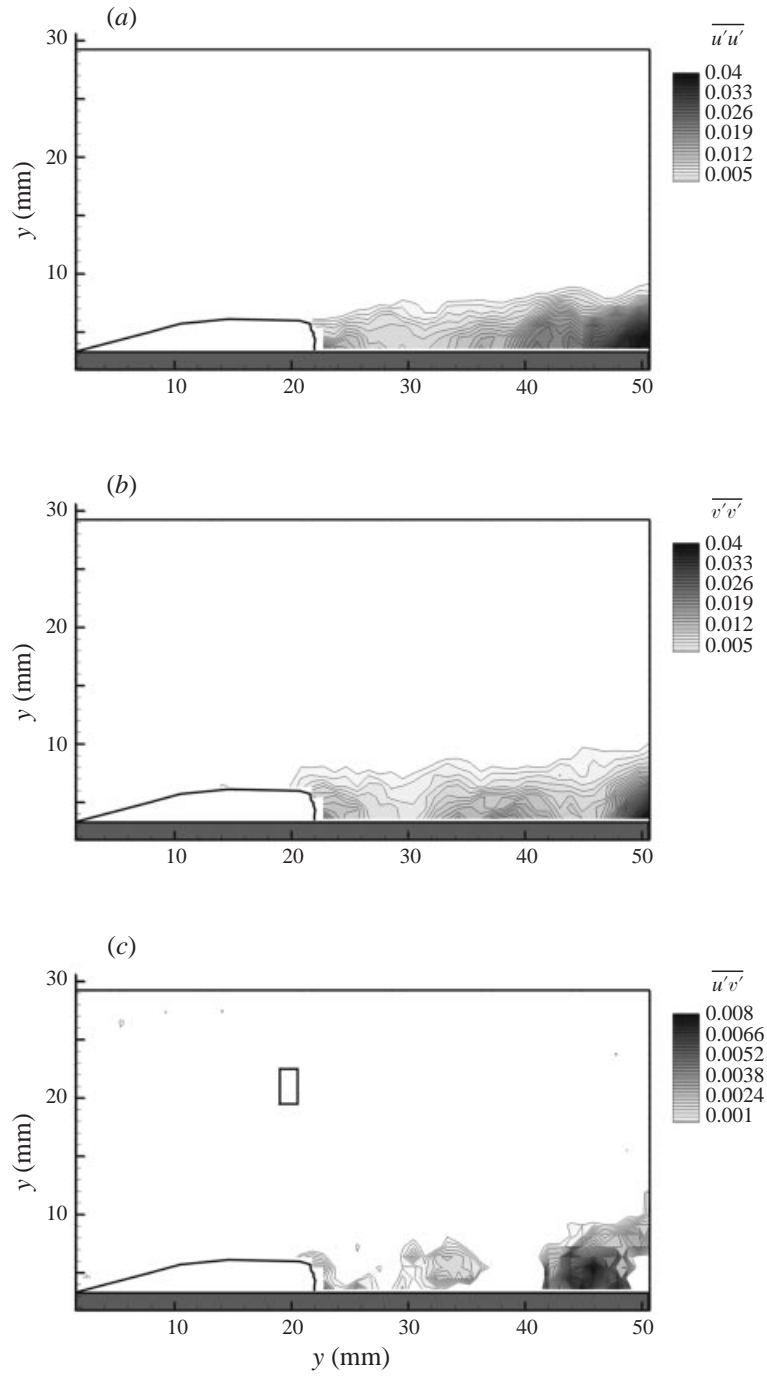
FIGURE 12. Reynolds stresses derived from 50 phase-averaged images of figure 11. Distribution of (*a*) $\overline{(u/u_o)'(u/u_o)'}$, (*b*) $\overline{(v/u_o)'(v/u_o)'}$, and (*c*) $\overline{(u/u_o)'(v/u_o)'}$. The rectangular region used to find the average u_o velocity component is shown in (*c*).
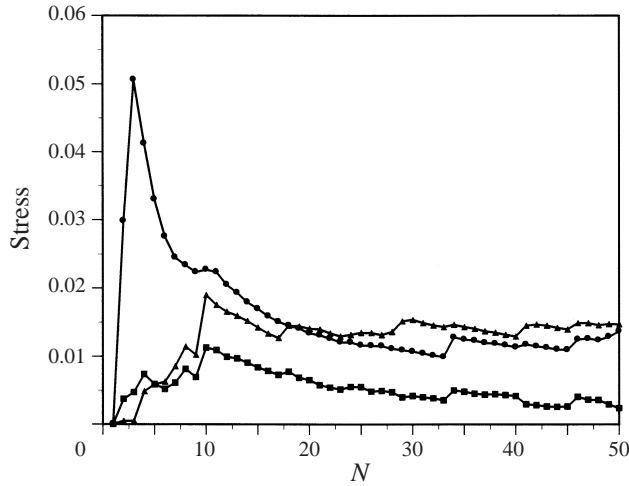
FIGURE 13. Convergence plots for the Reynolds stresses presented in figure 12. $\bullet$, $\overline{(u/u_o)'(u/u_o)'}$; $\blacktriangle$, $\overline{(v/u_o)'(v/u_o)'}$; and $\blacksquare$, $\overline{(u/u_o)'(v/u_o)'}$. N is the number of averaged images.

This was consistent with the Strouhal numbers for cloud shedding of two-dimensional open cavities of similar length (Kawanami *et al.* 1998).

Figure 14(*a*) presents the phase-averaged velocity field for a series of 50 images of cavities on the two-dimensional plano-convex hydrofoil at $\alpha = 2°$. Figure 14(*b*) shows the velocity field with the average velocity subtracted out, and figure 14(*c*) presents the corresponding averaged vorticity plot. The flow around the cavity on the two-dimensional plano-convex hydrofoil at $\alpha = 2°$ had similar characteristics to the flow around the cavity on the two-dimensional wedge. Figure 14(*d*) shows a contour plot of the square of the local average flow speed, $|\boldsymbol{u}|^2 = u^2 + v^2$. As in the cavity flow on the two-dimensional wedge, the pressure of the flow near the cavity surface reached a minimum near the middle of the cavity, where an adverse pressure gradient was observed. The pressure rose as the cavity terminus was reached.

Fluctuating components of the flow field were also determined for the series of 50 images. Figure 15(*c*) details the square region of the PIV image where the average u velocity component was measured in the manner described above. Figures 15(*a*), 15(*b*) and 15(*c*) present plots of the average Reynolds stresses, $\overline{(u/u_o)'(u/u_o)'}$, $\overline{(v/u_o)'(v/u_o)'}$, and $\overline{(u/u_o)'(v/u_o)'}$. The peaks of the normal stresses were approximately 10%, and the maximum average turbulent shear stress was approximately 30% of the maximum normal stresses. Figure 16 demonstrates the convergence of the Reynolds stresses at an arbitrary point located within the turbulent flow downstream of the cavity. The convergence is similar to that demonstrated in figure 13.

3.5. *Prediction of the cavity geometry on the wedges using free-streamline theory*

The cavity flow over the wedge was modelled using free-streamline theory. A description of this method can be found in Wu (1972). Simplifying assumptions were necessary to construct a solvable theoretical model, including the following:

(i) the flow was considered to be two-dimensional;

(ii) the cavity and its ensuing wake were separated from the outer flow by a free streamline;
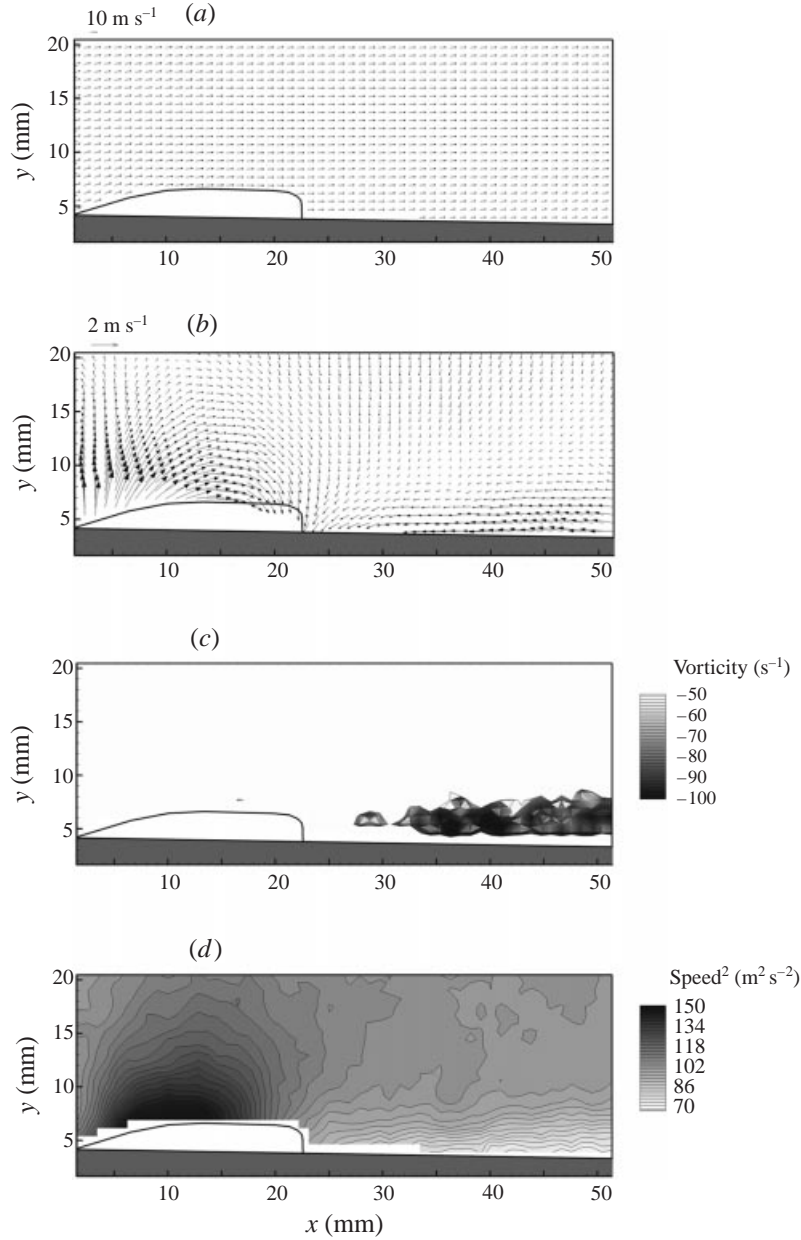
(iii) the outer flow was inviscid and irrotational;

10 m s^{-1} (*a*)

2 m s^{-1} (*b*)

(*c*)

Vorticity (s^{-1})
−50
−60
−70
−80
−90
−100

(*d*)

Speed^2 (m^2 s^{-2})
150
134
118
102
86
70

x (mm)

FIGURE 14. Averaged PIV velocity vector field on the two-dimensional, plano-convex hydrofoil. $\alpha = 2°$, $U = 9.5\,\mathrm{m\,s^{-1}}$, $\sigma = 0.77$. (*a*) Velocity field and (*b*) global mean subtracted from velocity field; $U_{gm} = 10.4\,\mathrm{m\,s^{-1}}$, $V_{gm} = 1.2\,\mathrm{m\,s^{-1}}$; (*c*) vorticity plot; (*d*) $|\boldsymbol{u}|^2 = u^2 + v^2$. 50 images were processed.

(iv) the specified constant cavity pressure determined the shape of the interface streamline;

(v) the fluid was assumed to be incompressible, even though both liquid and vapour phases were present;

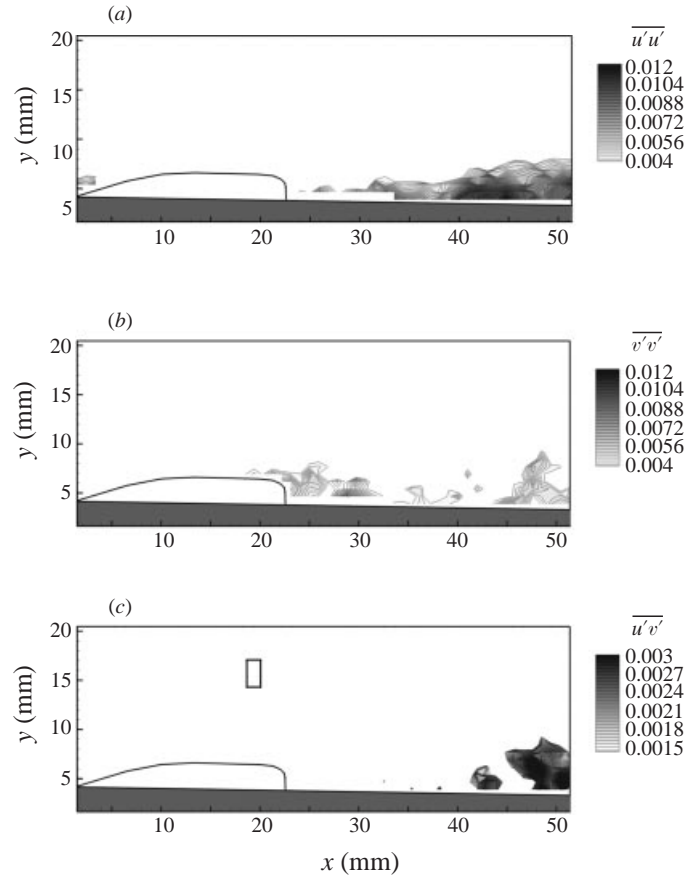(vi) the flow was assumed to be steady and the vortical flow behind the cavity was neglected;

FIGURE 15. Distribution of (a) $\overline{(u/u_o)'(u/u_o)'}$, (b) $\overline{(v/u_o)'(v/u_o)'}$; and (c) $\overline{(u/u_o)'(v/u_o)'}$, for the cavitating two-dimensional, plano-convex hydrofoil. $\alpha = 2°$, $U = 9.5\,\mathrm{m\,s^{-1}}$, $\sigma = 0.77$. 50 images were processed. The region used to find the average u_o velocity component is shown in (c).
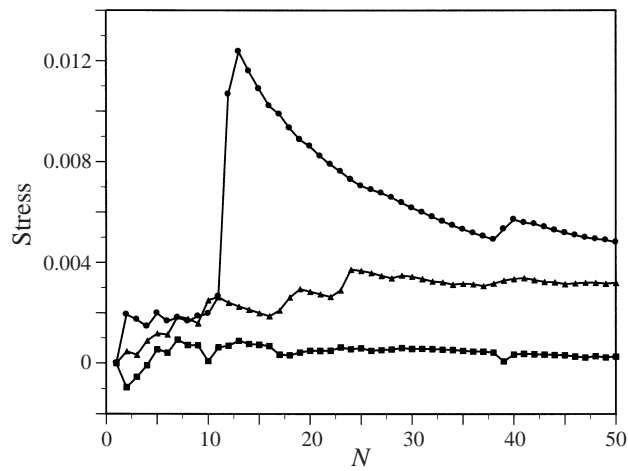

FIGURE 16. Convergence plots for the Reynolds stresses at an arbitrary point, $x = 33.5\,\mathrm{mm}$, $y = 5.5\,\mathrm{mm}$, behind the cavity on the two-dimensional, plano-convex hydrofoil. ●, $\overline{(u/u_o)'(u/u_o)'}$; ▲, $\overline{(v/u_o)'(v/u_o)'}$; ■, $\overline{(u/u_o)'(v/u_o)'}$.
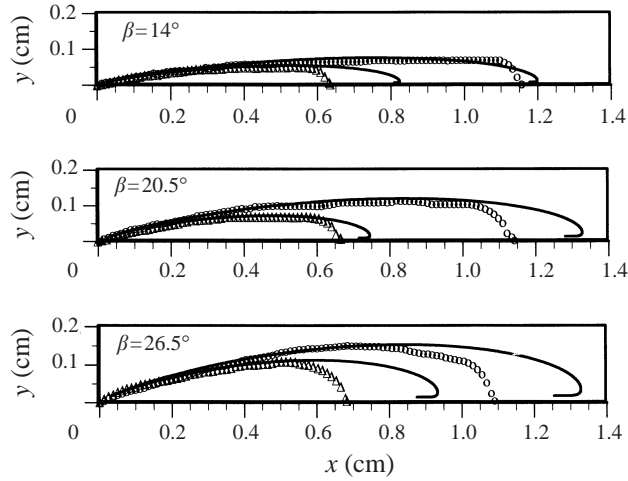
FIGURE 17. Experimentally measured and analytically predicted cavity profiles. Two profiles are plotted for each wedge. (a) $14°$ wedge, $\sigma_{exp} = 1.4$ and 1.7, $\sigma_{anal} = 1.67$ and 1.8; (b) $20.5°$ wedge, $\sigma_{exp} = 1.9$ and 2.1, $\sigma_{anal} = 2.07$ and 2.42; (c) $26.5°$ wedge, $\sigma_{exp} = 2.4$ and 2.7, $\sigma_{anal} = 2.46$ and 2.75. Uncertainty of σ is $\pm 6\%$.

(vii) a re-entrant flow was assumed to occur at the cavity closure, and the flux of liquid into the cavity was sunk within the cavity.

In the present study, the flow over the wedge was modelled, including the effect of the tunnel walls. A derivation is given in an Appendix. The model was used to predict the cavity geometry as a function of free-stream cavitation number.

Figure 9(a) shows the cavity length as a function of cavitation number for partial cavities forming at the vertex of the wedges. The experimental results and the results of the analytical model are shown. The solid line represents the predicted maximum length of the cavity, and the dashed line represents the predicted length of the cavity at the point of maximum cavity thickness. The measured cavity length was consistently shorter than the theoretical maximum length, lying closer to the cavity length at maximum thickness. Figure 9(b) shows the cavity length versus cavity thickness. The experimental data were scattered, but again, the data tended to fall closer to the line representing the cavity length at maximum thickness.

Typical cavity profiles are shown in figure 17. An analytical solution was found that matched the measured maximum cavity thickness, although the analytically determined cavitation number differed somewhat from the experimental conditions ($\sigma_{anal} > \sigma_{exp}$). The cavity profiles matched well up to the point of maximum cavity thickness, where the experimentally observed cavity was abruptly truncated. Note that the cavity length after the point of maximum thickness varies considerably, but the cavity length was never observed to grow to the predicted maximum length.

3.6. *Comparison of the open cavity flow to the flow behind a rearward facing step*

A comparison can be made between the flow near the closure of an open partial cavity, and a canonical flow, such as the rearward-facing step. Both are separated, turbulent shear flows. A schematic of the attached cavity and rearward-facing step comparison is shown in figure 18. Researchers have used the simple geometry of the rearward facing step to study the physics of single-phase turbulent shear flows, in particular the reattachment of separated turbulent shear layers. Kim, Line & Johnston (1980), Eaton
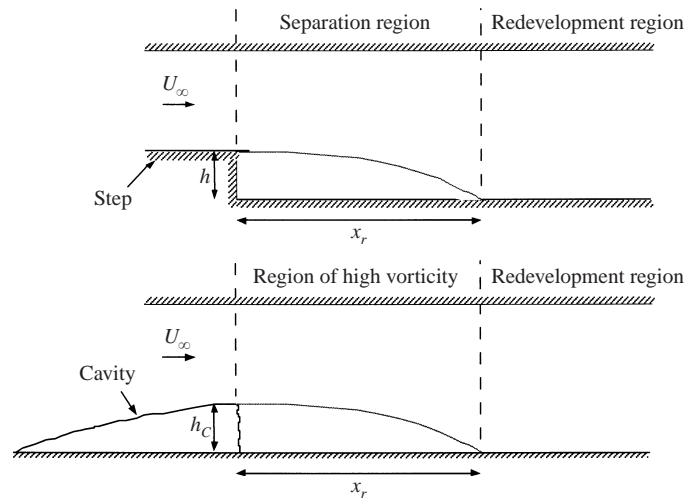
FIGURE 18. Schematic of rearward-facing step and attached cavity comparison.

& Johnston (1981), and Driver & Seegmiller (1985) studied incompressible turbulent flows over a rearward-facing step in channel flows at high Reynolds numbers. The velocity profile around the rearward-facing step and the reattachment distance of the separated flow behind the step were examined. Kim *et al.* (1980) showed that the maximum reverse velocity measured was approximately 25% of the free-stream velocity. Downstream of reattachment, the inner part of the velocity profile relaxes quickly, while the outer part requires a longer downstream distance. This produces an appreciable decrease in the mean velocity gradient, thus it does not follow the log law of the wall. Eaton & Johnston (1981) reviewed flows over a rearward-facing step in high-Reynolds-number flows with fully turbulent separated shear layers. They presented normalized velocity profiles from various experiments. Driver & Seegmiller (1985) performed velocity measurements using LDV. Kim *et al.* (1980) used tufts and a mixture of oils to examine flow separation and reattachment behind a rearward-facing step. The normalized mean reattachment distance, x_r/h_s, was determined to be 7 ± 1 when the flow is turbulent at separation; x_r is the flow reattachment length, and h_s is the height of the rearward-facing step. Eaton & Johnston (1981) reported in their review that x_r/h_s ranged from 4.9 to 8.2 Driver & Seegmiller (1985) inferred the reattachment length of the separated flow from both oil-flow laser interferometry measurements and thermal-tuft wall probes. The normalized reattachment length was found to be $x_r/h_s = 6.1 \pm 0.2$.

Rearward-facing steps with step heights of 0.16 cm, 0.32 cm, and 0.64 cm were constructed and tested in the BDWT to determine reattachment lengths behind the step for comparison with the two-dimensional, partial cavity. The boundary layer upstream of flow detachment was expected to be turbulent. The recirculation regions behind these three rearward-facing steps were visualized using the PIV images. These measurements fell within the reported limits of $x_r/h_s = 6.55 \pm 1.65$.

Measurements behind the step were compared to measurements in the wake of the open partial cavity. A strong, two-dimensional recirculation region was not observed behind the partial cavity as it was behind the rearward-facing step with a similar step height. The velocity vectors close to the wedge boundary at reattachment are approximately 60% of the free-stream velocity, compared to less than 25% in
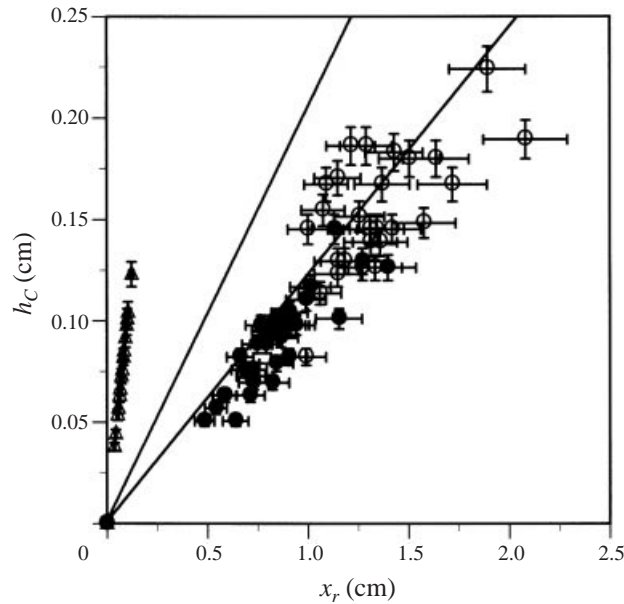
FIGURE 19. Cavity thickness, h_C, as a function of the reattachment length corresponding to the region of high vorticity downstream of the cavity, x_r: $\bigcirc$, 26.5° wedge; $\bullet$, 20.5° wedge; and $\triangle$, 14° wedge. The solid lines represent the limits of $x_r/h_C = x_r/h = 6.55 \pm 1.65$ which is the correlation between the reattachment length and the step height of a (non-cavitating) rearward-facing step.

the reattachment zone behind the rearward-facing step. This indicated that a more gradual velocity gradient existed in the closure region of the attached cavity than in the reattachment zone behind the rearward-facing step. The region of high vorticity behind the cavity, x_r, was compared to the reattachment distance behind the rearward-facing step, and was found to be of the same order. Figure 19 shows cavity thickness, h_C, versus the reattachment length, x_r. The normalized mean reattachment distance, x_r/h_C was approximately 9 for the 26.5° and the 20.5° wedges. These values were on the same order as the range of measurements presented by Kim *et al.* (1980), Eaton & Johnston (1981), and Driver & Seegmiller (1985) for the rearward-facing step.

The Reynolds stresses measured downstream of the cavity were on the order of those observed in the reattachment region of a rearward-facing step. The peaks of the normal stresses were approximately 10%, which was similar to those reported for non-cavitating shear layers. For example, Eaton & Johnston (1980) reported that the maximum fluctuation of the streamwise velocity component in the free shear layer behind a rearward-facing step was approximately 18% of the free-stream velocity at separation. The maximum average turbulent shear stress was approximately 30% of the maximum normal stresses, and this was equivalent to the average value reported for the non-cavitating shear flow behind a rearward-facing step.

The existence of a turbulent reattachment behind the cavity was consistent with the observations of Goldstein *et al.* (1970) of the separated flow behind a rearward-facing step. The relevant parameters of the step flow included the ratio of displacement thickness of the free shear layer near separation and the step height δ_s/h, and the Reynolds number of the separated shear flow $Re_h = U_s h/v$. They reported that for Reynolds numbers $Re_h > 500$ and $\delta_s/h < 0.4$, the reattachment process would be turbulent. For the cavity flows in this study, $Re_h \approx 1 \times 10^4$; the maximum cavity

thickness was taken to be analogous to the step height. The boundary layer thickness of the separated flow at the cavity terminus was not expected to be greater than 1×10^{-4} m, making $\delta_s/h \approx 1 \times 10^{-1}$. Thus, it was expected that the separated shear flow at the terminus of the open cavity would produce a turbulent flow that reattaches downstream of the cavity.

The open attached cavities were often observed to fill only a portion of the original non-cavitating separated region. The non-cavitating separated flows exhibited a *recirculating* flow within the separated region. However, reverse flow (i.e. flow in the upstream direction) was not observed in the reattachment region of the cavities formed on the planar geometries. Kim *et al.* (1980) reported that the magnitude of the reverse-flow velocity in the non-cavitating separated region behind a rearward-facing step is approximately 25% of the free-stream velocity. This flow was confined to a relatively thin surface layer near the downstream stagnation region (in a layer approximately 10% of the step height). In the closure region of partial attached cavities on these planar geometries, the instantaneous flow was three-dimensional and turbulent, so any reverse flow that existed would not be spatially coherent across the span and would be difficult to resolve with planar PIV. George *et al.* (2000) employed surface electrical probes to detect the near-surface stagnation flows within the bubbly region of the cavity closure for two-dimensional open cavities that were of similar geometry and appearance to those formed on the two-dimensional wedge in this study. A stagnation region often existed upstream of the visible cavity closure, within the bubbly mixture, and evidence of recirculation was found within these cavities. It is possible that recirculation existed within the optically opaque regions of the cavity that could not be observed with optical methods used in this study.

4. Results: partial cavities forming on the NACA0009 hydrofoil

The incipient and developed partial cavity flow occurring at the leading edge of the NACA0009 hydrofoil was examined. For these experiments, the angle of incidence, α, was varied from 5° to 8°. Smaller angles of incidence produced mid-chord cavitation instead of leading-edge cavitation. The nominal free-stream velocity was $9.2 \pm 0.4\,\mathrm{m\,s^{-1}}$, making the free-stream Reynolds number based on the hydrofoil chord length, $Re_L = U_\infty L/\nu$, equal to $(1.0 \pm 0.1) \times 10^6$. The range of cavitation numbers was 2.2 to 5.4. In contrast to the open partial cavities observed on the wedges and the plano-convex hydrofoil, the developed partial cavities on the NACA0009 hydrofoil were unsteady re-entrant cavities.

4.1. *Non-cavitating flow*

The non-cavitating flow near the leading edge of the two-dimensional, NACA0009 hydrofoil was examined using PSP, and an example is shown in figure 20(*a*). Neither PSP nor single-shot PIV images revealed leading-edge flow separation on the suction side of the hydrofoil for attack angles up to 8°.

4.2. *Cavity inception and appearance*

For attack angles α ⩾ 5°, attached cavities formed on the suction side of the NACA0009 hydrofoil near the leading edge. With decreasing cavitation number, incipient cavitation forms at the leading edge of the foil. With continued reduction in cavitation number, developed cavities form that are unsteady and shed large portions of the vapour-filled region creating cloud cavitation. These clouds are shed down-stream of the cavity and subsequently collapse. Figure 21 illustrates four images of
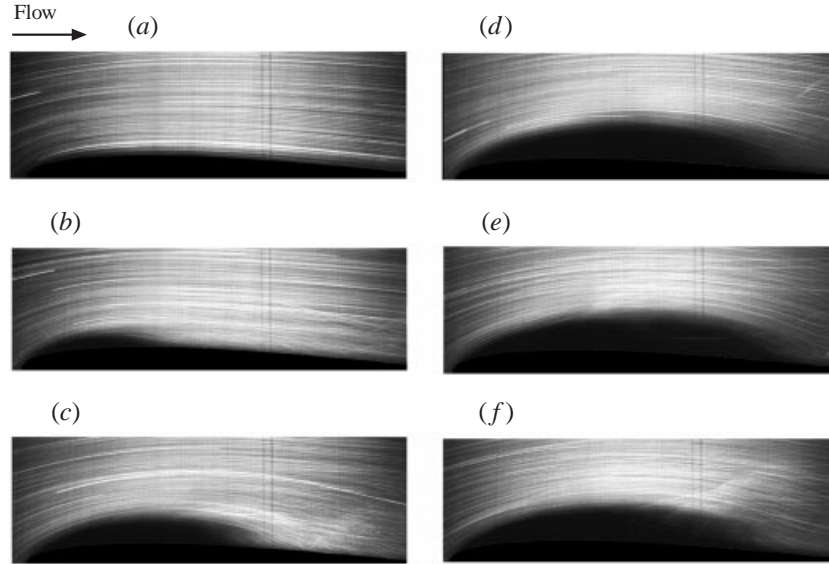
Flow →

(a)   (d)

(b)   (e)

(c)   (f)

FIGURE 20. Streak photography images of cavitation forming at the leading edge of the two-dimensional, NACA0009 hydrofoil at $\alpha = 8°$. (a) $U = 8.3\,\mathrm{m\,s}^{-1}$, $\sigma = 8.1$ (non-cavitating); (b) $U = 8.3\,\mathrm{m\,s}^{-1}$, $\sigma = 5.1$; (c) $U = 9.1\,\mathrm{m\,s}^{-1}$, $\sigma = 4.5$; (d) $U = 9.5\,\mathrm{m\,s}^{-1}$, $\sigma = 4.3$; (e) $U = 9.6\,\mathrm{m\,s}^{-1}$, $\sigma = 4.1$; (f) $U = 9.5\,\mathrm{m\,s}^{-1}$, $\sigma = 4.2$. The streamwise extent of the image is approximately 4 cm.

cavities forming on the NACA0009 hydrofoil at $\alpha = 7°$. Incipient cavities, developing cavities, cloud-shedding cavities, and filling cavities are illustrated.

The appearance of the cavities formed on the NACA0009 hydrofoil was considerably different from those formed on the wedges and the plano-convex hydrofoil. The vortical structures shed from the incipient cavities were smaller than the vortical structures shed from the cavities on the plano-convex hydrofoil and wedges. The variation in the spanwise lengths of the vortical structures was much narrower when compared to the broad range of lengths observed behind the open cavities on the plano-convex hydrofoil and the wedges. The classic filling and break-off cycle was observed for developed cavities on the NACA0009. When the cavity filled with re-entrant fluid, a large portion of the cavity that approximately spans the test section broke off and formed a cavitation cloud. The break-off occurred along a well-defined curved line, and a region of vapour-free fluid was seen between the separated cloud and the remaining partial cavity. This filling and break-off cycle of the cloud cavitation on the NACA0009 hydrofoil was periodic, with a shedding frequency of approximately 125 Hz (a Strouhal number of $St \approx 0.2$). This was somewhat lower than the values reported by Kawanami *et al.* (1998) for similar partial cavities. The significant area blockage of the hydrofoil (~ 25)% at $\alpha = 8°$ may have contributed to this difference.

Figure 20(b–f) shows streak photography images of the cavitation as it forms on the two-dimensional NACA0009 hydrofoil for $\alpha = 8°$. The cavity was very thin and the liquid flow reattached to the cavity without the production of a turbulent wake. The vortical wake downstream of these partial cavities was much thinner than the wake observed downstream of the open partial cavities forming on the plano-convex hydrofoil and the wedges.
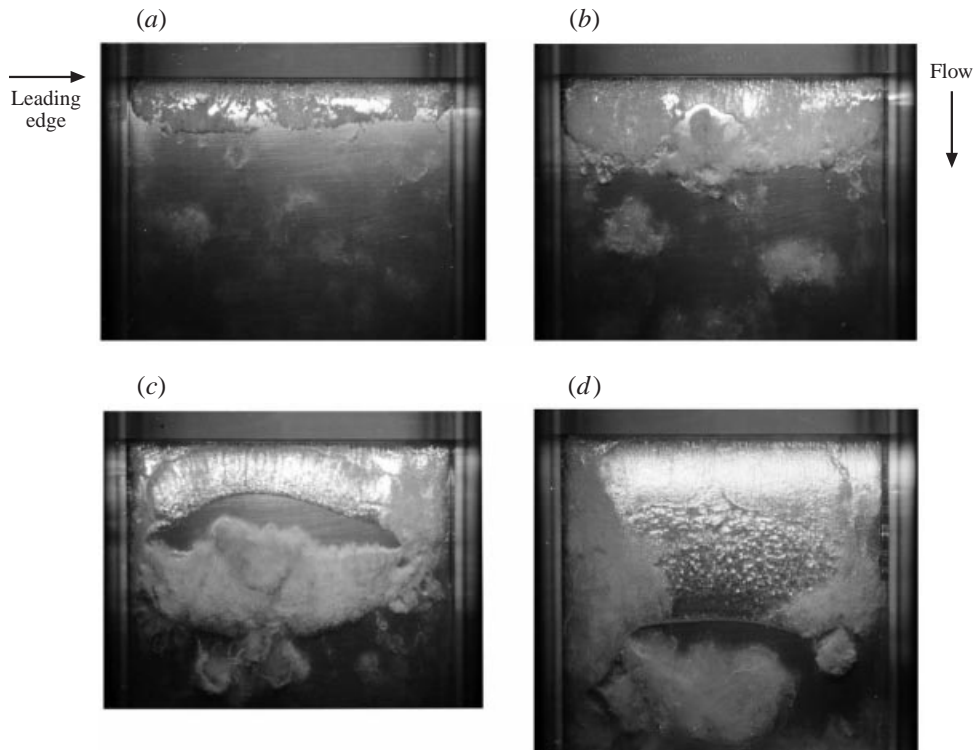
FIGURE 21. Cavitation on the two-dimensional NACA0009 hydrofoil $\alpha = 7°$. (*a*) Incipient, $U = 7.9\,\mathrm{m\,s}^{-1}$, $\sigma = 4.2$; (*b*) developing, $U = 8.1\,\mathrm{m\,s}^{-1}$, $\sigma = 3.6$; (*c*) cloud shedding, $U = 8.3\,\mathrm{m\,s}^{-1}$, $\sigma = 2.8$; (*d*) refilling, $U = 8.5\,\mathrm{m\,s}^{-1}$, $\sigma = 2.8$. Plan view.

4.3. *Cavity geometry*

The cavity thickness, h_C is plotted against cavity length, L_C, in figure 22. The thickness was taken as the maximum thickness of the cavity during the filling portion of the cloud shedding cycle. The cavities that form on the two-dimensional NACA0009 foil were much thinner than those on the two-dimensional plano-convex foil: h_C/L_C ranged from 0.08 to 1.16 for angles of incidence, α, of 5° to 8°. In addition, the streamlines around the cavity fared into the solid surface smoothly, producing little disturbance to the flow downstream of the cavity.

4.4. *Flow near the cavity and the closure region*

Cinemagraphic PIV was used to examine the flow field in the closure of the developed partial cavity on the NACA0009 hydrofoil as periodic cloud cavitation was produced. The method used to acquire and process the PIV data is the same as that described in § 3.4. Figure 23 presents the phase-averaged velocity fields for 50 images of cavities on the NACA0009 hydrofoil at $\alpha = 8°$. Four different portions of the cavity shedding cycle were examined: (*a*) cavity filling, (*b*) cavity break-off, (*c*) cloud roll-up, and (*d*) cloud collapse. The field of view for (*c*) and (*d*) was shifted downstream by 3 cm. The cavity boundary was conservatively defined to eliminate the portions of the image containing vapour and/or distorted particle images. Recirculating flow was not observed in the cavity wake. Figure 24 shows the velocity fields with the average velocity subtracted out. The average flow field in figures 24(*c*) and 24(*d*) reveals the circulating flow around the collapsing cloud and the strong mean shear of the flow
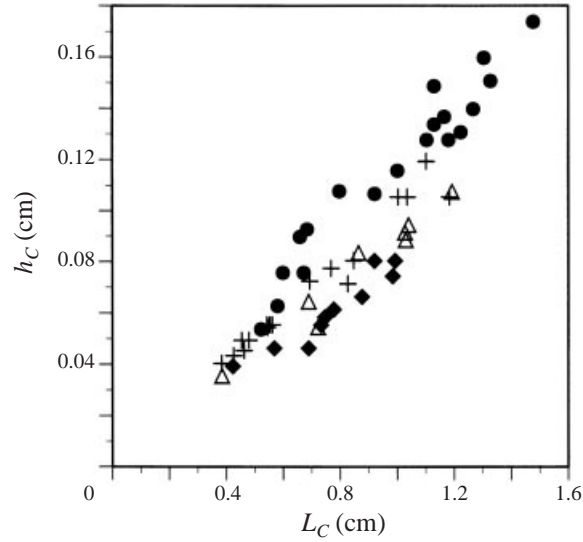
FIGURE 22. Plot of the cavity thickness, h_C, versus cavity length, L_C, for varying attack angles on the NACA0009 hydrofoil: $\blacklozenge$, $\alpha = 5°$; $\triangle$, $\alpha = 6°$; $+$, $\alpha = 7°$; $\bullet$, $\alpha = 8°$.
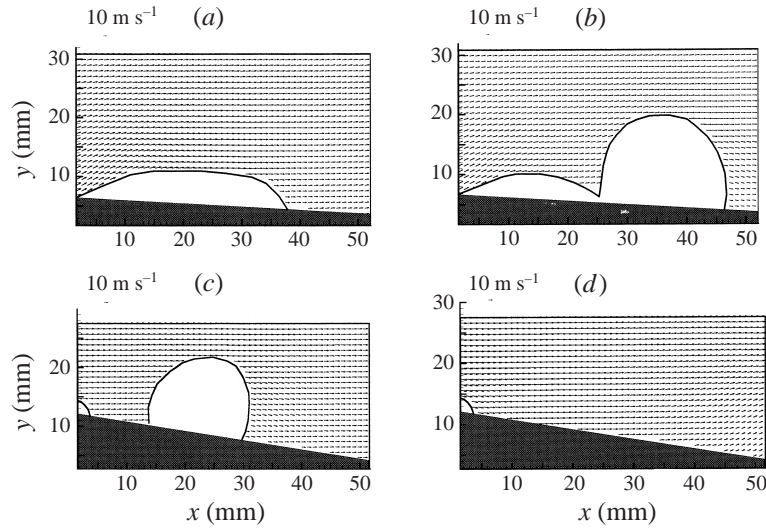

FIGURE 23. Averaged PIV velocity vector field on the two-dimensional, NACA0009 hydrofoil. $\alpha = 8°$, $U = 9.2\,\mathrm{m\,s^{-1}}$, $\sigma = 4.3$. (a) $t = 0\,\mu\mathrm{s}$, (b) $t \approx 3500\,\mu\mathrm{s}$, (c) $t \approx 5500\,\mu\mathrm{s}$, (d) $t \approx 8000\,\mu\mathrm{s}$. 50 images were processed at each stage.

after the collapse of the cloud. After the collapse, a stagnation-like flow can be seen where the cloud collapsed. Figure 25 presents the corresponding averaged vorticity plot. The flow remained largely irrotational until the cavitation cloud collapsed. The wall-bounded shear flow remained thin downstream of the cavity and cannot be resolved with the PIV.

Figure 26 shows a contour plot of the square of the local average flow speed, $|\boldsymbol{u}|^2 = u^2 + v^2$. Because the flow is largely irrotational, the local pressure can be found from the local speed through application of the Bernoulli equation. However,
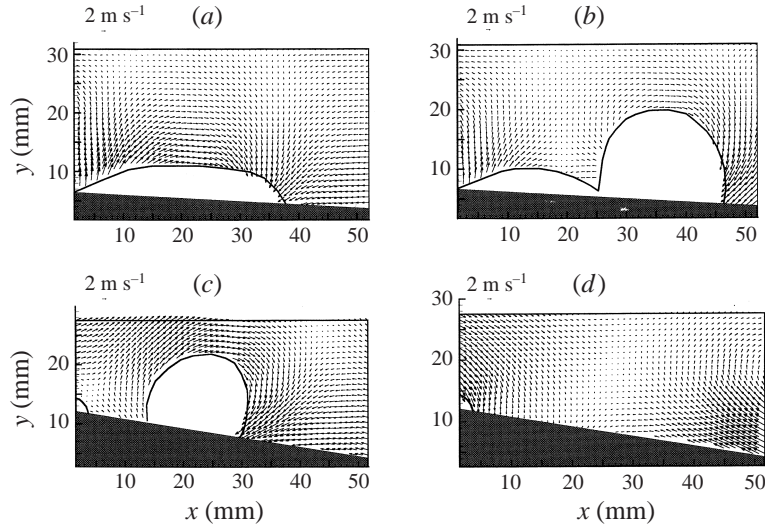
FIGURE 24. Global mean vectors subtracted from the averaged PIV velocity vector field on the two-dimensional, NACA0009 hydrofoil. $\alpha = 8°$, $U = 9.2\,\mathrm{m\,s^{-1}}$, $\sigma = 4.3$. (a) $t = 0\,\mu\mathrm{s}$, $U_{gm} = 15.8\,\mathrm{m\,s^{-1}}$, $V_{gm} = 2.1\,\mathrm{m\,s^{-1}}$; (b) $t \approx 3500\,\mu\mathrm{s}$, $U_{gm} = 15.9\,\mathrm{m\,s^{-1}}$, $V_{gm} = 2.9\,\mathrm{m\,s^{-1}}$; (c) $t \approx 5500\,\mu\mathrm{s}$, $U_{gm} = 13.9\,\mathrm{m\,s^{-1}}$, $V_{gm} = -0.1\,\mathrm{m\,s^{-1}}$; (d) $t \approx 8000\,\mu\mathrm{s}$, $U_{gm} = 13.4\,\mathrm{m\,s^{-1}}$, $V_{gm} = 1.1\,\mathrm{m\,s^{-1}}$. 50 images were processed at each stage.

the flow here is unsteady, and application of the Bernoulli equation will yield the approximate local flow coefficient, C_P,

$$C_P \approx 1 - \frac{|\boldsymbol{u}|^2}{U_\infty^2} - \frac{2}{U_\infty^2} \int_l \frac{\partial |\boldsymbol{u}|}{\partial t}\,\mathrm{d}s.$$

The acceleration of the 'outer flow' near the detachment point of the cavity is $\Delta |\boldsymbol{u}|/\Delta t \approx 1 \times 10^2\,\mathrm{m\,s^{-2}}$. The unsteady term of the Bernoulli equation is approximated to be

$$\frac{2}{U_\infty^2} \int_l \frac{\partial |\boldsymbol{u}|}{\partial t}\mathrm{d}s \approx \frac{2}{U_\infty^2} \frac{\Delta |\boldsymbol{u}|}{\Delta t}\Delta s \approx 0.2,$$

where $\Delta s \approx 1 \times 10^{-1}$ and $U_\infty \approx 1 \times 10^1$. Typical values of $|\boldsymbol{u}|^2/U_\infty^2$ ranged from 0 to 5. Therefore, the local pressure would be modified by approximately 5% to 20% due to flow unsteadiness. The speed data can be used to qualitatively examine the pressure field. During the cavity filling process, the pressure near the cavity surface reached a minimum near the middle of the cavity where an adverse pressure gradient is observed. This was similar to the pressure field observed near the open partial cavities on the wedges and the plano-convex hydrofoil. A pressure rise downstream of the cavity was observed, which is responsible for the collapse of the cavitation cloud.

Figures 27, 28, and 29 present plots of the average Reynolds stresses. Overall, the turbulent fluctuations of the flow were small. The turbulence and vorticity within the flow were concentrated in the region of cavitation cloud collapse. The maximum turbulent intensity of the normal stresses was approximately 25%, which was twice as high as the value observed for the wake behind the open partial cavity on the two-dimensional wedge and plano-convex hydrofoil. The maximum average turbulent shear stress was approximately 60% of the maximum normal stresses, which indicated that the turbulence in this region was highly anisotropic. The convergence plots for
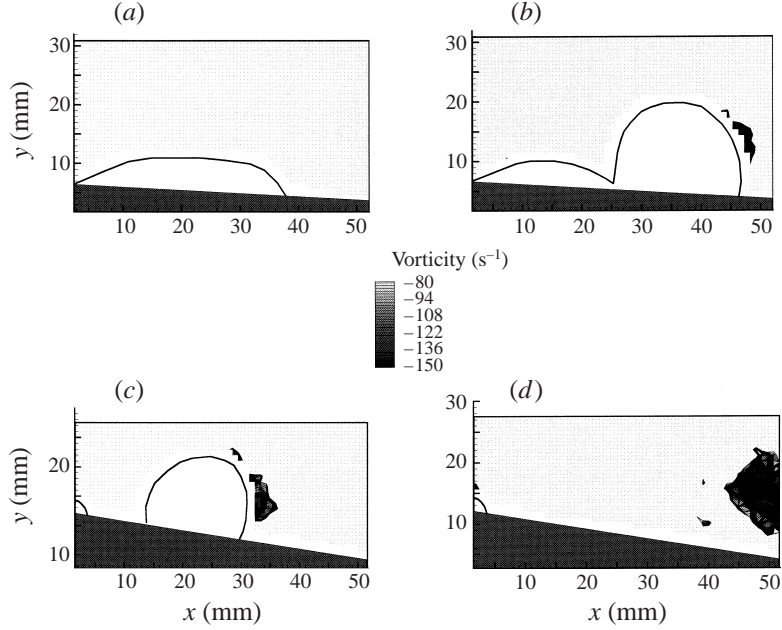
FIGURE 25. Vorticity plots for the cavitating two-dimensional, NACA0009 hydrofoil. $\alpha = 8°$, $U = 9.2\,\mathrm{m\,s}^{-1}$, $\sigma = 4.3$. (a) $t = 0\,\mu\mathrm{s}$, (b) $t \approx 3500\,\mu\mathrm{s}$, (c) $t \approx 5500\,\mu\mathrm{s}$, (d) $8000\,\mu\mathrm{s}$. 50 images were processed at each stage.

the Reynolds stresses at an arbitrary point located downstream of the cavity and corresponding cloud break-off at the four time intervals are shown in figure 30.

4.5. *Generation of vorticity*

High vorticity was found in the vicinity of the cloud collapse. The cross-sectional area of this region was approximately equivalent to the cross-sectional area of the original cavitating cloud. If there is circulation around the original cloud, its magnitude, Γ, is given by the following:

$$\Gamma = 2\pi R U_T = \pi R^2 \bar{\omega}_C,$$

where R is the approximate radius of both the cavitating cloud and the circular region of high vorticity observed after the cloud collapsed, and U_T is the average tangential speed of the rotating cavitation cloud. If this circulation was preserved after the cloud collapse, the average spanwise vorticity in the post-collapse region, $\bar{\omega}_C$, would be equal to $\Gamma/\pi R^2$. The measured average of the in-plane vorticity found in the flow after the collapse of the cavitation cloud was $\bar{\omega}_C \approx -150\,\mathrm{s}^{-1}$. With $R \approx 7\,\mathrm{mm}$, this would imply a circulation of $\Gamma \approx -0.02\,\mathrm{m^2\,s}^{-1}$, and tangential speed of $U_T \approx 0.5\,\mathrm{m\,s}^{-1}$ (with the cloud rotation in the clockwise direction).

Alternatively, it is possible that baroclinic torques were responsible for the production of vorticity during the collapse of the cloud, since density gradients within the cloud were not necessarily aligned with the pressure gradients around the cloud during collapse. Considering the flow as a continuum, the production of baroclinic vorticity is related to the pressure and density gradients in the flow:

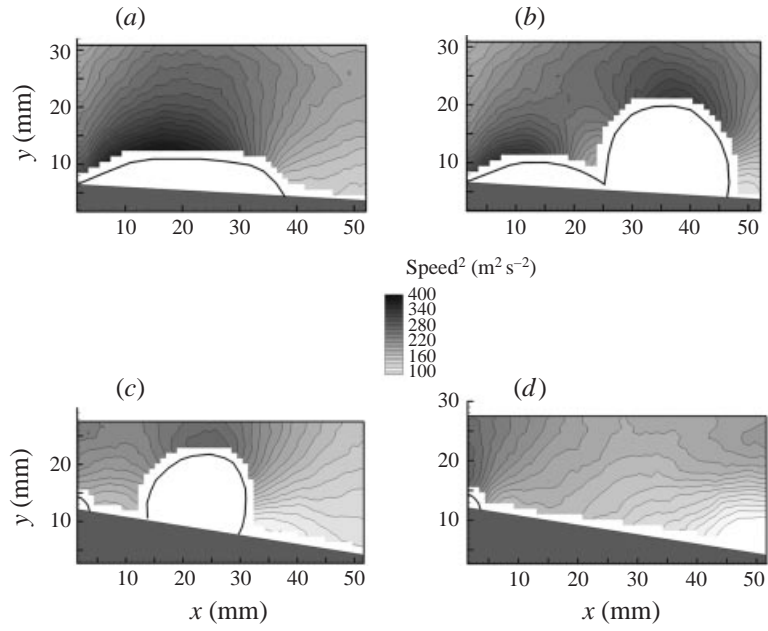$$\frac{\mathrm{D}\omega_C}{\mathrm{D}t} \approx \frac{1}{\rho_C^2}\nabla\rho_C \times \nabla P$$

FIGURE 26. $|\boldsymbol{u}|^2 = u^2 + v^2$ plot for the cavitating two-dimensional, NACA0009 hydrofoil. $\alpha = 8°$, $U = 9.2\,\mathrm{m\,s^{-1}}$, $\sigma = 4.3$. (a) $t = 0\,\mu s$, (b) $t \approx 3500\,\mu s$, (c) $t \approx 5500\,\mu s$, (d) $8000\,\mu s$. 50 images were processed at each stage.
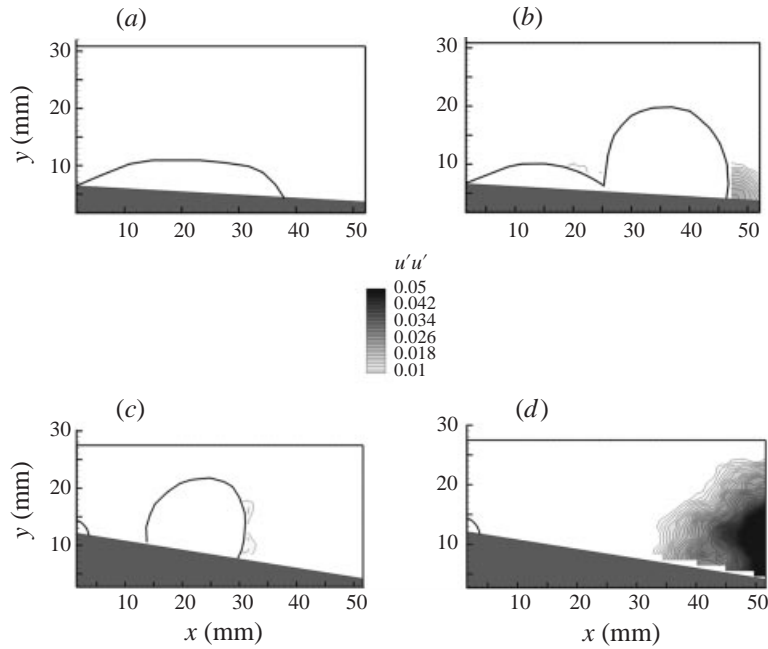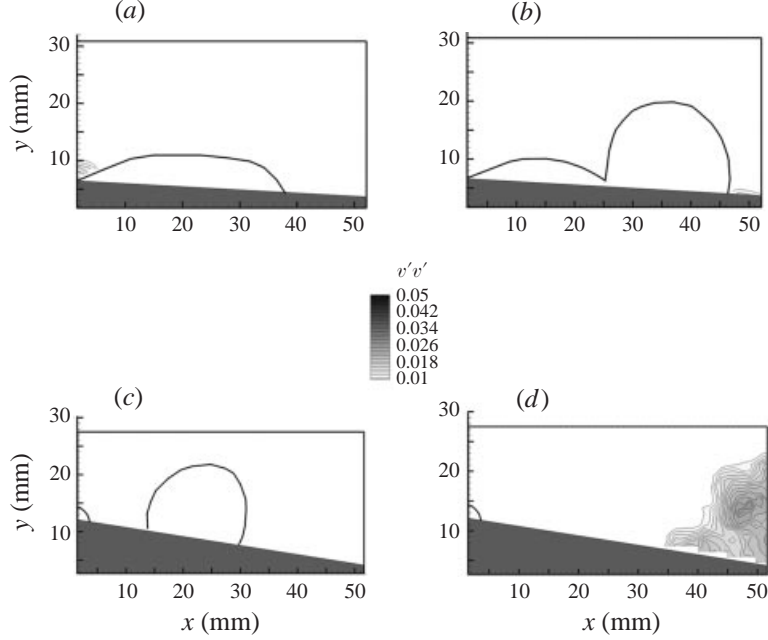

FIGURE 27. Distribution of $\overline{(u/u_o)'(u/u_o)'}$ for the two-dimensional, NACA0009 hydrofoil. $\alpha = 8°$, $U = 9.2\,\mathrm{m\,s^{-1}}$, $\sigma = 4.3$. (a) $t = 0\,\mu s$, (b) $t \approx 3500\,\mu s$, (c) $t \approx 5500\,\mu s$, (d) $t \approx 8000\,\mu s$. 50 images were processed at each stage.

FIGURE 28. As figure 27 but for $\overline{(v/u_o)'(v/u_o)'}$.

where $\rho_C = \rho(1 - \alpha)$ is the density of the bubbly cloud mixture and α is the void fraction of the bubbly cloud. The vorticity produced during cloud collapse scales in the following way:

$$|\bar{\omega}_C| \sim \left| \frac{1}{\rho(1-\alpha)^2} \nabla\alpha \times \nabla P \cdot t_C \right| \approx \frac{1}{R_C^2} \alpha_M U_M^2 t_C,$$

where t_C is the duration of cloud collapse. The largest pressure gradients across the cloud are $\nabla P \approx -\frac{1}{2}\rho\nabla(U^2) \approx -\frac{1}{2}\rho(U_M^2)/2R_C$ with $U_M^2 \approx 10^2\,\mathrm{m^2\,s^{-2}}$. The gradient of the void fraction is approximately $\nabla\alpha \approx \alpha_M/R_C$, where α_M is the maximum void fraction at the centre of the cloud. α_M was estimated to be between 1% and 10% (Maeda *et al.* 1991, and Yu & Ceccio 1997), and R_C was on the order of $10^{-2}\,\mathrm{m}$. The cloud collapse time was on the order of $10^{-3}\,\mathrm{s}$. Thus, the largest magnitude of the produced vorticity would be on the order of 10 to $100\,\mathrm{s^{-1}}$. This was consistent with the measured value of $\bar{\omega}_C \approx -150\,\mathrm{s^{-1}}$. However, the measured sign of the average vorticity after cloud collapse was uniformly negative, and it was possible that baroclinically produced vorticity could lead to the generation of vorticity of both positive and negative sign, depending on the local orientation of the pressure and void fraction gradients during collapse.

5. Discussion

Two types of developed cavities were observed on these two-dimensional text objects: open partial cavities on the wedges and the plano-convex hydrofoil and unsteady re-entrant partial cavities on the NACA0009 hydrofoil. The significant differences between the cavity dynamics on these test objects can be ascribed to the existence or absence of re-entrant flow at the cavity closure. It is therefore important to examine under what conditions significant re-entrant flow will or will not occur.
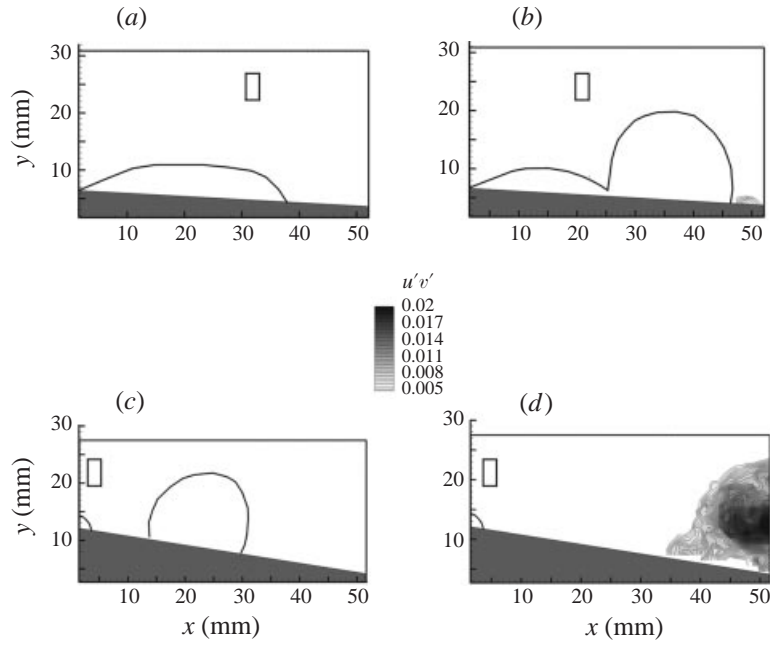
$u'v'$
0.02
0.017
0.014
0.011
0.008
0.005

FIGURE 29. As figure 27 but for $\overline{(u/u_o)'(v/u_o)'}$. The region used to find the average u_o velocity component is shown at each stage.
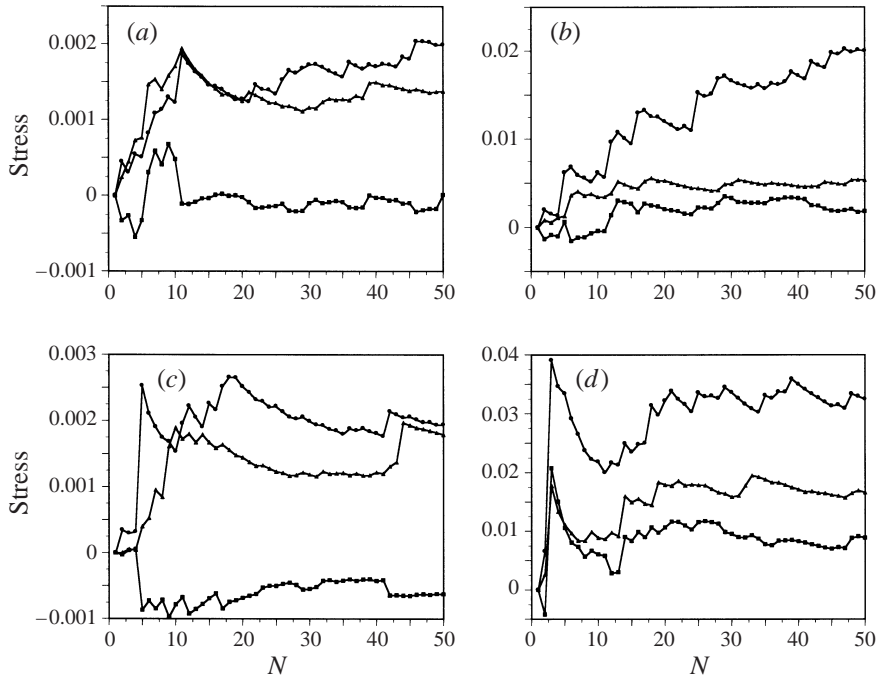

FIGURE 30. Convergence plots for the Reynolds stresses at an arbitrary point behind the cavity on the two-dimensional, NACA0009 hydrofoil: ●, $\overline{(u/u_o)'(u/u_o)'}$; ▲, $\overline{(v/u_o)'(v/u_o)'}$; ■, $\overline{(u/u_o)'(v/u_o)'}$. (a) $t = 0\,\mu$s, $x = 43.4$ mm, $y = 6.6$ mm; (b) $t \approx 3500\,\mu$s, $x = 49.2$ mm, $y = 6.6$ mm; (c) $t \approx 5500\,\mu$s, $x = 43.0$ mm, $y = 9.2$ mm; (d) $t \approx 8000\,\mu$s, $x = 43.0$ mm, $y = 9.2$ mm.
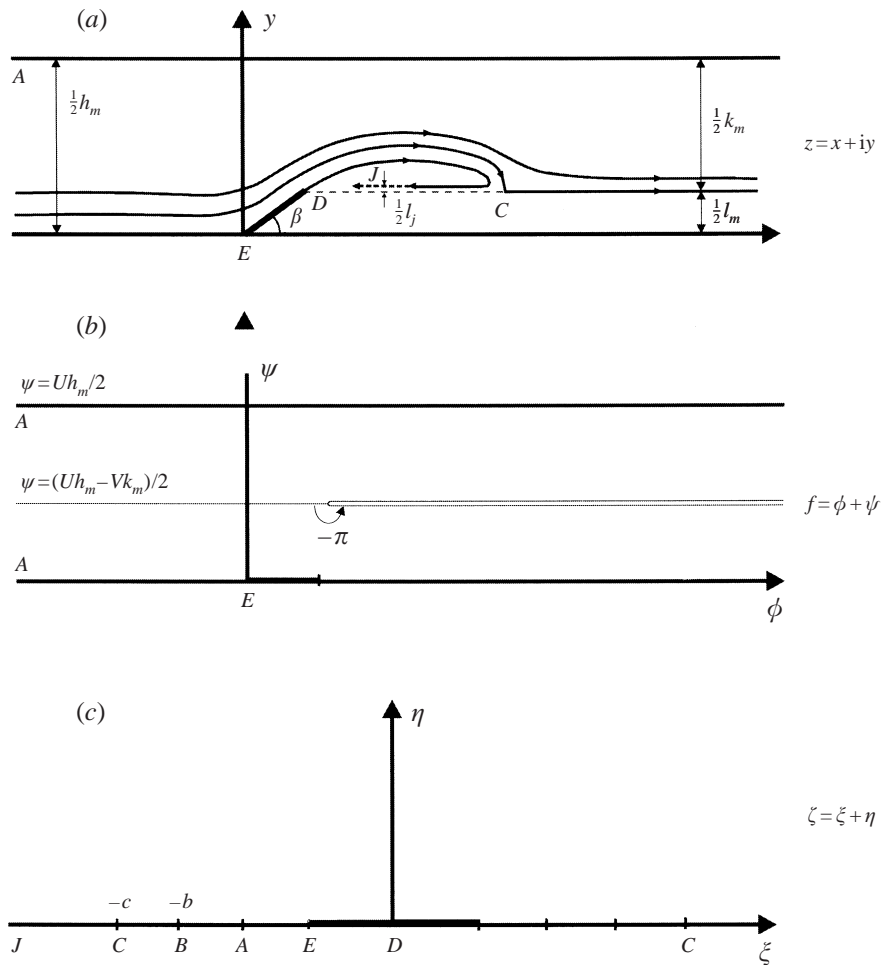
FIGURE 31. Potential cavity flow in (*a*) the physical *z*-plane, (*b*) the complex potential *f*-plane, and (*c*) parametric ζ-plane.

An idealized description of partial cavity closure is often referred to as the 're-entrant jet model'. The surface of the partial cavity closes back on itself to form a thin jet of fluid that enters the cavity (this is the cavity closure condition employed in the free-streamline model presented in the Appendix). Such a closure can be termed a *laminar* cavity closure. The flow in the closure of the unsteady re-entrant partial cavities exhibited such a laminar reattachment. As the cavity formed, grew, filled, and shed, the flow remained attached to the cavity surface, and remained virtually irrotational excluding the region of cloud-cavitation collapse. Conversely, the open partial cavities exhibited a *turbulent* cavity closure. The cavity profile expected from the free-streamline model was observed for only a portion of the cavity, with predicted and observed cavity profiles matching up to the region of maximum cavity thickness, at which point the experimentally observed cavity terminated. Only a small portion of the cavity near the detachment region was completely vapour filled, while the remainder consisted of a bubbly mixture of vapour and liquid. A turbulent shear flow existed downstream of the maximum extent of the open partial cavity. While this shear flow contained some bubbles and vapour-filled vortices, the void fraction

of the flow downstream of the cavity closure was very low compared to that of the bubbly mixture within the cavity. The separated flow behind the cavity is expected to be fully turbulent.

Why did these partial cavities close with a truncated, turbulent wake? Examination of the velocity magnitude near the cavity interface revealed that adverse pressure gradients exist near the terminus of both open and re-entrant partial cavities. It is often assumed that the cavity interface is a constant-pressure surface. However, mass and momentum transport across the interface can lead to a difference in pressure across the gas–liquid boundary of a steady partial cavity. If the interface is stationary, the balance of mass and momentum at the interface yield the following relationships:

$$\rho V_{L,n} = \rho_v V_{v,n},$$

$$P_L - P_v = -\kappa\gamma + \rho_v V_{v,n}^2 - \rho V_{L,n}^2,$$

where $V_{v,n}$ and $V_{L,n}$ are the velocity components normal to the interface of the vapour and liquid flow, ρ_v is the density of the vapour, and γ is the interfacial tension, $P_L - P_v$ is the pressure difference across the interface. Combining these relationships (and neglecting surface tension) yields

$$P_L - P_v = V_{L,n}^2 \rho \left(\frac{\rho}{\rho_v} - 1\right).$$

If there is no mass transport across the interface, there will be no pressure across it. With mass transport, a pressure difference can exist and is related to the normal component of the liquid velocity. Only a small amount of mass transport is needed to produce a measurable pressure difference. For example, a pressure difference of 1 to 10 kPa would result if the normal velocity component of the liquid were on the order of 0.03 to 0.10 m s^{-1}. However, the vapour velocity normal to the interface would be on the order of 10^4 times the liquid velocity due to the difference in liquid and vapour density, and it is not expected that these high gas velocities occur within the cavity. Measurements close to the interface suggest that the liquid pressure near the cavity closure could be as much as 10 kPa higher than the cavity pressure, but limitations in spatial resolution did not permit measurement of liquid velocities extremely close to the interface. A re-examination of the open partial cavities indicates that only a portion of the cavity interface near the detachment point is a continuous gas–liquid surface, with the majority of the cavity being composed of a bubbly mixture. This gas–liquid mixture is not necessarily in thermodynamic equilibrium, and the liquid pressure outside this bubbly region can be higher than the vapour pressure despite the presence of collapsing vapour bubbles. Small bubbles in the wake of the open cavities will take a finite amount of time to collapse as they convect away from the closure of the cavity into regions of increased pressure. In this case, the bubbly cavity boundary would not necessarily be a constant-pressure interface.

If adverse pressure gradients near the closure of the closed cavities are not sufficient to collapse the cavity, the cavity flow can remain largely attached and a re-entrant jet can form. In contrast, the shear flow in the closure of open cavities occurred because an adverse pressure gradient in the flow near the cavity interface caused the cavity to collapse. The open cavities terminated near the point of maximum cavity thickness, where the free-stream pressure began to rise. The resulting liquid shear layer produced a turbulent reattachment.

6. Conclusions

The cavity flows examined in the present study are canonical in nature, but they reveal interesting phenomena that are instructive about cavitation that forms on more complex geometries. Because the cavity boundary is not necessarily a constant-pressure interface, it is possible that adverse pressure gradients near the wake of the cavity can lead to the 'premature' condensation of the cavity and the formation of a turbulent wake. Alternatively, the cavity surface may ultimately close to form a re-entrant flow. The influence of pressure gradients on the dynamics of partial cavities has also been observed by Callenaere, Franc & Michel (1998) for partial cavities forming downstream of a step.

A non-constant pressure at the cavity interface has implications for the modelling of partial cavity flows. If it is assumed that the cavity interface is a constant-pressure surface, the model will predict a cavity with a laminar reattachment with accompanying re-entrant flow. Such cavities exist when the adverse pressure gradients near the cavity closure do not lead to significant mass transport (condensation) across the cavity boundary. However, strong pressure gradients in the flow can lead to significant mass transport, and ultimately, the re-condensation and truncation of the cavity and the creation of a turbulent cavity wake. Of course, the pressure near the cavity is strongly coupled to the cavity geometry as well as to the remaining overall flow field. Therefore, prediction of which type of cavity will occur for a given flow configuration requires prediction of the entire cavitating flow field and may not be readily apparent *a priori*.

Appendix. A free-streamline model of the two-dimensional cavity flow

The following model is based on that of Wu, Whitney & Brennen (1971), and a review is provided by Wu (1972). Consider a partial cavity forming at the vertex of a wedge. The velocity potential of the flow is $V = \nabla\phi(u = \partial\phi/\partial x, v = \partial\phi/\partial y)$. For an incompressible fluid the continuity equation is $\nabla \cdot V = 0$. Therefore, for incompressible, irrotational flows, it follows that the velocity potential $\phi(x, t)$ satisfies the Laplace equation, $\nabla^2 \phi = 0$. The velocity component perpendicular to the solid surfaces must be zero. On the cavity boundary, described by $F(x, t) = 0$, the kinematic boundary condition is

$$\frac{\mathrm{D}F}{\mathrm{D}t} = \frac{\partial F}{\partial t} + (\nabla\phi) \cdot \nabla F = 0 \quad \text{on} \quad F(x, t) = 0.$$

For the dynamic boundary condition, it is assumed that the pressure on the cavity boundary, $P = p_C$, is constant. The effects of gravity and surface tension are neglected. The unsteady Bernoulli equation is used to find the dynamic boundary condition:

$$\frac{\partial\phi}{\partial t} + \tfrac{1}{2}(\nabla\phi)^2 = \tfrac{1}{2}U_\infty^2(1 + \sigma) \quad \text{on} \quad F(x, t) = 0,$$

where $\sigma = (P_\infty - p_C)/\tfrac{1}{2}\rho U_\infty^2$ is the cavitation number.
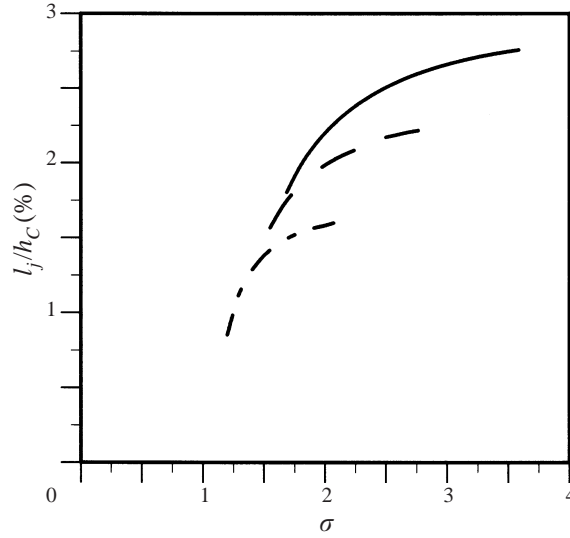
FIGURE 32. Analytically predicted re-entrant jet thickness as a function of the cavitation number, σ, where l_j is the thickness of the re-entrant jet and h_C is the cavity thickness. Solutions for the 26.5° wedge (solid line), 20.5° wedge (dashed line), and 14° wedge (long–short dashed line) are shown.

The detachment point where the free streamline leaves the solid surface is fixed at the vertex of the wedge with vertex angle β. The cavity streamline detaches with a continuous slope. A closure model must be specified and the re-entrant closure scheme was chosen (see figure 31a). A stagnation point exists downstream of the cavity, and a finite portion of the inlet flow forms a jet that flows into the cavity. It is assumed in the model that this jet flow is sunk within the cavity and does not impinge on the interface.

The solution presented here follows that of Wu *et al.* (1971). Figure 31(a) shows a schematic of the potential flow solution. Three parameters define the problem in the physical plane defined by $z = x + iy$: the free-stream cavitation number, $\sigma = 1/U^2 - 1$, the blockage ratio of the wedge, $\lambda = l_m/h_m$, and the wedge vertex angle, β. The normalized velocity U is equal to U_∞/q_C where q_C is the (constant) flow speed at the cavity interface. The steady incompressible potential cavity flow in the physical plane is represented with the complex velocity potential $f = \phi + i\psi$, where ϕ is the velocity potential, and ψ is the stream function. The corresponding regions in the z- and f-planes are shown in figures 31(b) and 31(c). The complex velocity potential, f, and the complex velocity, w, are analytic functions of z. The complex velocity is defined by

$$w = \frac{\mathrm{d}f}{\mathrm{d}z} = u - iv = |w|e^{-i\theta},$$

where $|w| = \sqrt{u^2 + v^2}$ is the flow speed and $\theta = \tan^{-1}(v/u)$. A logarithmic hodograph variable ω is used instead of w, which is defined by

$$\omega = \log[q_C/w] = \tau + i\theta,$$

where

$$\tau = \log q_C/|w|$$

and

$$\theta = \tan^{-1}(v/u).$$

The constant flow speed on the cavity boundary q_C is set equal to unity. The hodograph variable is defined such that $\tau = 0$ on the cavity interface, and θ is equal to the angle of flow at the boundaries.

The analytical solution of the cavity flow over the wedge is determined in a parametric form, using the complex velocity potential $f = f(\zeta)$ and the hodograph variable $\omega = \omega(\zeta)$, where $\zeta = \xi + i\eta$ is a suitable complex variable. The flow region in the f-plane is mapped conformally onto the real axis of the hodograph plane ζ by the generalized Schwartz–Christoffel transformation:

$$\frac{\mathrm{d}f}{\mathrm{d}\zeta} = \frac{A\zeta(\zeta^2 - c^2)}{(\zeta^2 - a^2)(\zeta^2 - b^2)}.$$

By this formula, f can be continued analytically into the entire ζ-plane (by virtue of $\mathrm{Im}\, f = 0$ on $\xi = 0$). The wetted surface is mapped onto $\eta = 0$, $-1 < \xi < 1$, and the stagnation point onto the origin of ζ. From the singular behaviour of f, at $\zeta = a, b$, and ∞, it follows that

$$f(\zeta = a) = \pi i \frac{p(a)}{q'(a)} = \pi i \frac{A(c^2 - a^2)}{2(b^2 - a^2)}.$$

In the f-plane at $\zeta = a$,

$$f(\zeta = a) = \tfrac{1}{2} U h_m i$$

and therefore,

$$U h_m = \pi A \left(\frac{c^2 - a^2}{b^2 - a^2} \right) \quad \text{at } \xi = a,\ z = A.$$

Similarly,

$$f(\zeta = b) = -\tfrac{1}{2} V k_m i$$

and therefore

$$V k_m = \pi A \left(\frac{c^2 - b^2}{b^2 - a^2} \right) \quad \text{at } \xi = b,\ z = B.$$

Boundary conditions for the hodograph variable $\omega = \tau + i\theta$ are determined as follows:

$$
\begin{aligned}
\theta^+(\xi) = \theta(\xi, +0) &= -\pi & (\xi < -c) & \quad \text{along } CJ, \\
&= 0 & (-c < \xi < -1) & \quad \text{along } EABC, \\
&= \beta(\xi) & (-1 < \xi < 0) & \quad \text{along } ED, \\
\tau(0, \eta) &= 0 & (\eta > 0). &
\end{aligned}
$$

These boundary conditions in the physical plane are mapped into the hodograph plane. The function $\omega(\zeta)$ is continued analytically into the first quadrant of the ζ-plane by $\omega(-\bar{\zeta}) = -\overline{\omega(\zeta)}$. A Reimann–Hilbert problem is solved, and the solution of $\omega(\zeta)$ is given by the Poisson integral,

$$\omega(\zeta) = \frac{1}{\pi} \int_{-\infty}^{+\infty} \frac{\theta^+(\xi)}{\xi - \zeta} \mathrm{d}\xi = \log\left(\frac{c - \zeta}{c + \zeta} \right) + \frac{1}{\pi} \int_{-1}^{1} \frac{\beta(\xi)}{\xi - \zeta} \mathrm{d}\xi.$$

Since $\beta(\xi) = \beta\pi = \text{constant}$ for a two-dimensional wedge, $\omega(\zeta)$ becomes.

$$\omega(\zeta) = \log\left(\frac{c - \zeta}{c + \zeta} \right) \left(\frac{\zeta - 1}{\zeta + 1} \right)^{\beta}.$$

The complex velocity then becomes

$$w(\zeta) = e^{-\omega(\zeta)} = \left(\frac{c + \zeta}{c - \zeta}\right)\left(\frac{\zeta + 1}{\zeta - 1}\right)^{\beta}.$$

At points A and B, respectively,

$$\zeta \to -a, w \to U, \quad \zeta \to -b, w \to V,$$

such that

$$U(a, b) = \left(\frac{c(a, b) - a}{c(a, b) + a}\right)\left(\frac{a - 1}{a + 1}\right)^{\beta}, \quad V(a, b) = \left(\frac{c(a, b) - b}{c(a, b) + b}\right)\left(\frac{b - 1}{b + 1}\right)^{\beta},$$

where

$$c(a, b) = \frac{k(a, b)b - a}{1 - k(a, b)}, \quad k(a, b) = \frac{1}{\sqrt{1 - \lambda(a, b)}}\left(\frac{a - 1}{a + 1}\right)^{\beta/2}\left(\frac{b + 1}{b - 1}\right)^{\beta/2}, \quad \lambda(a, b) = \frac{l_m}{h_m}.$$

The solution in the physical planes is given by

$$z(\zeta, a, b) = \int_{-1}^{\zeta} \frac{1}{w}\frac{df}{d\zeta}d\zeta = \frac{b^2 - a^2}{c^2(a, b) - a^2}\frac{U(a, b)h_m}{\pi}\int_{-1}^{\zeta} \frac{-\zeta(\zeta - c(a, b))^2}{(\zeta^2 - a^2)(\zeta^2 - b^2)}\left(\frac{\zeta - 1}{\zeta + 1}\right)^{\beta}d\zeta.$$

Point D corresponds to $\zeta = 0$ and $\mathrm{Im}\, z(\zeta = 0) = l_m/2$:

$$\lambda(a, b) = \mathrm{Im}\left[\frac{b^2 - a^2}{c^2(a, b) - a^2}\frac{2U(a, b)}{\pi}\int_{-1}^{0} \frac{-\zeta(\zeta - c(a, b))^2}{(\zeta^2 - a^2)(\zeta^2 - b^2)}\left(\frac{\zeta - 1}{\zeta + 1}\right)^{\beta}d\zeta\right].$$

After mapping and solving the Riemann–Hilbert problem for a given β, the solution is represented by two constants a, b. These parameters are determined through the simultaneous solution of the relationships of $U(a, b)$ and $\lambda(a, b)$, in conjunction with the restraint that $a > 1$ and $b > a$. Determination of a and b for a given U and λ requires iteration.

The cavity streamline is defined by the locus of points $0 < \mathrm{Im}(\zeta) < \infty$ and $\mathrm{Re}(\zeta) = 0$. With this streamline defined, the cavity profile, length, and thickness can be determined. The re-entrant jet thickness is given by

$$l_j(a, b) = \tfrac{1}{2}[U(a, b) - (1 - \lambda(a, b))V(a, b)].$$

Thus, a solution of the two-dimensional cavity flow on a wedge is completely determined. Results of the model are presented in figure 9 (cavity length and maximum thickness versus cavitation number) and figure 17 (cavity profiles). The thickness of the re-entrant jet versus the cavitation number is shown in figure 32.

REFERENCES

ADRIAN, R. J. 1991 Particle-image techniques for experimental fluid mechanics. *Ann. Rev. Fluid Mech.* **23**, 261–304.

AVELLAN F., DUPONT P. & RYHMING I. 1988 Generation mechanism and dynamics of cavitation vortices downstream of a fixed leading edge cavity. *Proc. 17th ONR Symp. on Naval Hydrodynamics*, pp. 317–329.

BREWER, W. & KINNAS, S. 1997 Experiment and viscous flow analysis on a partially cavitating hydrofoil. *J. Ship Res.* **41**, 161–171.

CALLENAERE, M., FRANC, J.-P. & MICHEL, J.-M. 1998 Influence of cavity thickness and pressure gradients on the unsteady behaviour of partial cavities. *Proc. Third Intl Symp. on Cavitation, Grenoble*, Vol. 1, pp. 209–214.

DONG, R., CHU, S. & KATZ, J. 1992 Quantitative visualization of the flow within the volute of a centrifugal pump. *Trans. ASME: J. Fluids Engng* **114**, 390–395.

DRIVER, D. M. & SEEGMILLER, H. L. 1985 Features of a reattaching turbulent shear layer in divergent channel flow. *AIAA J.* **23**, 163–171.

EATON, J. K. & JOHNSTON, J. P. 1981 A review of research on subsonic turbulent flow reattachment. *AIAA J.* **19**, 1093–1100.

FRANC, J. P. & MICHEL, J. M. 1985 Attached cavitation and the boundary layer: experimental investigation and numerical treatment. *J. Fluid Mech.* **154**, 63–90.

GEORGE, D. L., IYER, C. O. & CECCIO, S. L. 2000 Measurement of the bubbly flow beneath partial attached cavities using electrical impedance probes. *Trans. ASME: J. Fluids Engng* **122**, 151–155.

GINDROZ, B. & BILLET, M. L. 1994 Nuclei and propeller cavitation inception. *Proc. Symp. on Cavitation and Gas–Liquid Flow in Fluid Machinery and Devices.* ASME FED-Vol. 190, pp. 251–260.

GOLDSTEIN, R. J., ERIKSEN, V. L., OLSON, R. M. & ECKERT, E. R. G. 1970 Laminar separation, reattachment, and transition of the flow over a downstream-facing step. *Trans. ASME: J. Basic Engng* December, 732–741.

KAWANAMI, Y., KATO, H. & YAMAGUCHI, H. 1998 Three-dimensional characteristics of the cavities formed on a two-dimensional hydrofoil. *Proc. Third Intl Symp. on Cavitation, April 1998, Grenoble, France* (ed. J. M. Michel & H. Kato), pp. 191–196.

KAWANAMI, Y., KATO, H., YAMAGUCHI, H., TANIMURA, M. & TAGAYA, Y. 1997 Mechanism and control of cloud cavitation. *Trans. ASME: J. Fluids Engng.* **119**, 788–795.

KIM, J., LINE, S. J. & JOHNSTON, J. P. 1980 Investigation of reattachment of a turbulent shear layer: Flow over a backward-facing step. *Trans. ASME: J. Fluids Engng* **102**, 302–308.

KNAPP, R. T. 1955 Recent investigations of the mechanics of cavitation and cavitation damage. *Trans. ASME* **77**, 1045–1054.

KUBOTA, A., KATO, H., YAMAGUCHI, H. & MAEDA, M. 1989 Unsteady structure measurement of cloud cavitation on a foil section using conditional sampling technique. *Trans. ASME: J. Fluids Engng* **111**, 204–210.

LABERTEAUX, K. L. 1998 Flow in the closure region of partial attached cavitation. PhD thesis, University of Michigan, Ann Arbor, Michigan.

LABERTEAUX, K. L, CECCIO, S. L., MASTROCOLA, V. J. & LOWRANCE, J. L. 1998 High speed digital imaging of cavitating vortices. *Exps. Fluids* **24**, 489–498.

LANGE, D. F. DE 1996 Observation and modelling of cloud formation behind a sheet cavity. PhD thesis, University of Twente, The Netherlands.

LARRARTE, F., PAUCHET, A., BOUSQUET, P. & FRUMAN, D. H. 1995 On the morphology of natural and ventilated cavities. *Proc. ASME Symp. on Cavitation and Multiphase Flow.* ASME FED, Vol. 210 (ed. J. Katz & Y. Matsumoto), pp. 31–38.

LE, Q., FRANC, J. P. & MICHEL, J. M. 1993*a* Partial cavities: global behavior and mean pressure distribution. *Trans. ASME: J. Fluids Engng* **115**, 243–248.

LE, Q., FRANC, J. P. & MICHEL, J. M. 1993*b* Partial cavities: pressure pulse distribution around cavity closure. *Trans. ASME: J. Fluids Engng* **115**, 249–254.

LIU, Z. C. & ADRIAN, R. J. 1993 Simultaneous imaging of the velocity fields of two phases. In *Particulate Two-Phase Flow* (ed. M. C. Roco), pp. 33–58. Butterworth–Heinemann.

LUSH, P. A. & SKIPP, S. R. 1986 High speed cine observations of cavitating flow in a duct. *Intl J. Heat Fluid Flow* **7**, 283–290.

MAEDA, M., YAMAGUCHI, H. & KATO, H. 1991 Laser holography measurements of bubble populations in cavitation cloud on a foil surface. *ASME Cavitation '91 Symp.*, Vol. 116, pp. 67–75.

PEREIRA, F. 1997 Prédiction de L'érosion de cavitation: Approche énergétique. PhD thesis, École Polytechniques Fédérale de Lausanne, Lausanne.

PHAM, T. M., LARRARTE, F. & FRUMAN, D. H. 1998 Investigation of unstable cloud cavitation. In *Proc. Third Intl Symp. on Cavitation, April 1998, Grenoble, France*, pp. 215–220.

REISMAN, G. E. & BRENNEN, C. E. 1996 Pressure pulses generated by cloud cavitation. *Proc. ASME Symp. on Cavitation and Gas–Liquid Flows in Fluid Machinery and Devices.* FED Vol. 236 (ed. S. L. Ceccio, A. Furukana & J. H. Kim), pp. 319–328.

SRIDHAR, G. & KATZ. J. 1994 The effect of bubble clouds on vortex rings. *ASME Cavitation and Multiphase Flow*, Lake Tahoe. FED, Vol. 194 (ed. J. Katz), pp. 35–37.

STUTZ, B. & REBOUD, J. L. 1997 Experiments on unsteady cavitation. *Exps. Fluids* **22**, 191–198.

TASSIN, A. L., LI, C.-Y, CECCIO, S. L. & BERNAL, L. P. 1995 Velocity field measurements of cavitating flows. *Exps. Fluids* **20**, 125–130.

WU, T. Y. 1972 Cavity and wake flows. *Ann. Rev. Fluid Mech.* **4**, 243–284.

WU, T. Y., WHITNEY, A. K. & BRENNEN, C. 1971 Cavity-flow wall effects and correction rules. *J. Fluid Mech.* **49**, 223–256.

YU, P. W. & CECCIO, S. L. 1997 Diffusion induced bubble populations downstream of a partial cavity. *Trans. ASME: J. Fluids Engng* **119**, 782–787.

ZHANG, Y., GOPALAN, S. & KATZ, J. 1998 On the flow structure and turbulence in the closure region of attached cavitation. In *22nd ONR Symp. on Naval Hydrodynamics*, pp. 227–238.